The 2004 tectonic and hydrothermal crisis in the Danakil depression: documenting the last continental step prior to oceanic spreading

Daniel Mège[1], Ernst Hauber[2], Pascal Allemand[3], Hugo Moors[4], Mieke de Craen[5], Hanjin Choe[6], and Jérôme Dyment[7]

[1]Centrum Badan Kosmicznych PAN
[2]DLR
[3]Laboratoire de Géologie de Lyon - OSU de Lyon
[4]SCK•CEN
[5]Belgian Nuclear Research Centre
[6]Kangwon National University
[7]IPGP

November 22, 2022

Abstract

The Danakil depression in Ethiopia, at the end of the southern Red Sea, has been the locus of volcanic crises in 2004-10, with emplacement of 15 dykes: one, non-emergent, in Lake Asale next to Black Mountain and south of the Dallol dome during fall 2004, the others in the Dabbahu-Manda Hararo rift segment between September 2005 and May 2010. We report on a hydrothermal crisis that opened a 4.5 km long fissure in the ground, at the same time the Black Mountain dyke was intruding the crust 2 km away and parallel to it. The fissure, located north and south of Yellow Lake (Gaet'ale) and trending NNW-SSE, is still active. Its morphology is remarkably diversified, but surface evidence of the structural deformation has been lost over the years. Its formation is coeval with the intrusion of the Black Mountain dyke intrusion. It is suggested that after its documented propagation, the Black Mountain dyke propagated aseismically eastward as a sill, disrupting the stress equilibrium in the long-living Yellow Lake hydrothermal environment. The stress field was brought to rupture by the increased deviatoric stress, triggering the nucleation of a tensile fracture that propagated to the surface and released the far-field stress already released at depth by the emplacement of the dyke. This study documents the delicate intermingling of magmatic, tectonic, and hydrothermal processes at the ultimate step of continental rifting prior to the earliest stage of oceanic spreading.

Supplementary Material 4

Uninterpreted Figure 10

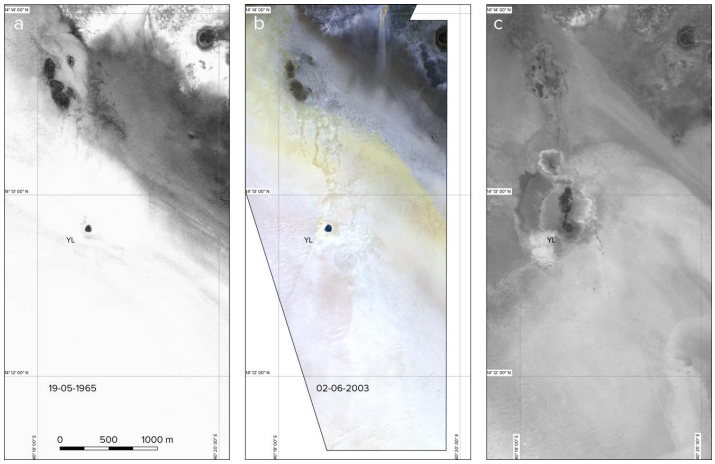

Structural evolution of the Yellow Lake Fissure area since 1965. The black lines are fracture lines either exposed to the surface, along which pools are sometimes located, or linear salt plate edge alignments suggestive of deeper tension fracturing or fracturing at subcritical stress. YL stands for Yellow Lake. Left: fracturing already observed in 1965 by KeyHole 4-A (2.4m/pixel, image ID); middle: additional fracturing observed in 2003 by Quickbird-2 multispectral (2m/pixel; Gram-Schmidt pansharpened to 0.5 m/pixel); right: fracturing observed since the first post-YLF high-resolution satellite image, by OrbView-3 (1m/pixel), in 2005.

Supplementary Material 1

1. Description of the material used in Supplementary Material 2 (video): Evolution of the YLF area between August 26th, 2004 and December 3rd 2005.

The Landsat-7 image composites show bands 8 (red), 7 (green) and 5 (blue), and the ASTER image composites show band 1 (red), 6 (green) and 4 (blue). The image IDs are:

Date	Scene ID (Landsat-7)/Local granule ID (ASTER)
2004-08-26	LE71680502004239ASN01
2004-09-11	LE71680502004255ASN01
2004-09-27	LE71680502004271ASN01
2004-10-13	LE71680502004287ASN01
2004-11-14	LE71680502004319ASN00
2005-01-01	LE71680502005001PFS00
2005-01-17	LE71680502005017ASN00
2005-02-02	LE71680502005033ASN00
2005-02-18	LE71680502005049ASN00
2005-04-07	AST_L1T_00304072005075551_20150508235844_19664 and AST_L1T_00304072005075600_20150508235850_118442
2005-04-23	AST_L1T_00304232005075553_20150509044713_121936 and AST_L1T_00304232005075602_20150509044735_103448
2005-06-10	LE71680502005161ASN00
2005-07-28	LE71680502005209ASN00
2005-08-13	LE71680502005225ASN00
2005-08-29	LE71680502005241ASN00
2005-09-14	LE71680502005257ASN00
2005-09-30	LE71680502005273ASN00
2005-12-03	LE71680502005337SGS00

2. IDs of the other products used in this paper

Date	Satellite or mission	Product ID
1965-05-19	KeyHole-4A	DS1021-1009DA051
1972-05-08	KeyHole-4B	DS1117-2041DF151
2001-10-21	Landsat-7	LE71680502001294SGS00
2003-06-02	Quickbird-2	03JUN02074523-M2AS-012368508010_01_P002
2004-11-14	ASTER	AST_08_00311142004075459_20200406124521_16810
2005-01-19	ASTER	AST_08_00301092005193545_20200406124451_16620
2005-02-17	ASTER	AST_08_00302172005194137_20200406124451_16622
2005-12-17	OrbView-3	3v051217p0001021551a520005700852m_001625696_1GST
2012-11-15	Pleaides-1A	DS_PHR1A_201211150755134_SE1_PX_E040N14_0405_01880
2015-03-17	Spot-6	DS_SPOT6_201503170724335_FR1_FR1_FR1_FR1_E040N14_01709
2016-07-02	Pleiades-1B	DS_PHR1B_201607020802006_FR1_PX_E040N14_0306_04448
2016-11-20	WorldView-2	A010010600B3E700
2017-10-21	Pleaides-1A	DS_PHR1A_201710210751425_FR1_PX_E040N14_0403_04941
2018-01-13	Landsat-8	LC81680502018013LGN00
2019-01-24	Pleiades-1B	DS_PHR1B_201901240803060_FR1_PX_E040N14_0406_01048
2019-02-26	Pleiades-1B	DS_PHR1B_201902260758313_FR1_PX_E040N14_0406_01124

The 2004 tectonic and hydrothermal crisis in the Danakil depression: documenting the last continental step prior to oceanic spreading

Daniel Mège

Solar System Dynamics and Planetology Group, Space Research Centre, Poland, dmege@cbk.waw.pl

Ernst Hauber

Institute of Planetary Research, German Aerospace Centre (DLR), Berlin, Germany

Pascal Allemand

Geology Laboratory, Claude-Bernard University ,Lyon, France

Hugo Moors, Mieke de Craen

Belgian Nuclear Research Centre, Mol, Belgium

Hanjin Choe

Research Institute for Earth Resources, Kangwon National University, Chuncheon, Korea

Jérôme Dyment

CNRS, Institute of Earth Physics (IPGP), Paris, France

Abstract

The Danakil depression in Ethiopia, at the end of the southern Red Sea, has been the locus of volcanic crises in 2004-10, with emplacement of 15 dykes: one, non-emergent, in Lake Asale next to Black Mountain and south of the Dallol dome during fall 2004, the others in the Dabbahu-Manda Hararo rift segment between September 2005 and May 2010. We report on a hydrothermal crisis that opened a 4.5 km long fissure in the ground, at the same time the Black Mountain dyke was intruding the crust 2 km away and parallel to it. The fissure, located north and south of Yellow Lake (Gaet'ale) and trending NNW-SSE, is still active. Its morphology is remarkably diversified, but surface evidence of the structural deformation has been lost over the years. Its formation is coeval with the intrusion of the Black Mountain dyke intrusion. It is suggested that after its documented propagation, the Black Mountain dyke propagated aseismically eastward as a sill, disrupting the stress equilibrium in the long-living Yellow Lake hydrothermal environment. The stress field was brought to rupture by the increased deviatoric stress, triggering the nucleation of a tensile fracture that propagated to the surface and released the far-field stress already released at depth by the emplacement of the dyke. This study documents the delicate intermingling of magmatic, tectonic, and hydrothermal processes at the ultimate step of continental rifting prior to the earliest stage of oceanic spreading.

1. Introduction

Due to the harsh conditions and regional politically instability, the geology of the northern Danakil depression has not been much studied in the last decades in spite of its remarkable tectonic setting,

at the boundary between the Nubian Plate and the Danakil Block, a transitional microplate between the Nubian Plate in the West and the Arabian Plate in the East (Figure 1).

The last major magmatic-tectonic event occurred there in October-November 2004, when a dyke intruded the Danakil rift parallel to its axis in the Asale dry lake, just south of the Dallol dome and east of Black Mountain (Figure 2). The Black Mountain dyke intruded the crust at a depth of 2-6 km, over a lateral distance of 9 km, with a maximum opening of 5 m at depth ~4 km. A Mogi source was identified at a close distance to the centre of the Dallol dome, at depth 1.5-3.3 km (Nobile et al., 2012). Several months earlier, a dyke had intruded the Erta'ale 75 km south of the Black Mountain dyke (Barnie et al., 2016a), but its small size, extent, and shallowness make it difficult to connect to the crustal dilation materialised by the Black Mountain dyke. A year later and 175 km to the South, in September 2005, a dyke intrusion event occurred south of the Dabbahu volcano, at the northern end of the Manda Hararo rift, and gave birth to a spectacular elongated vent (Wright et al., 2005). It was followed by 13 other dyke intrusions, including three eruptive, along the Manda Hararo rift (Belachew et al., 2011), the last intrusion occurring in May 2010 (Barnie et al., 2016b). Dyke depth was from 0 km or shallow to 10 km, and length between 10 and 60 km, with a maximum opening of 0.7 to 3.1 m (Ebinger et al., 2010 for the 13 first intrusions; Barnie et al., 2016b for the last intrusion). Additionally, a deep (6-12 km), 6 km long dyke, 1.5 m wide, intruded the crust 460 km to the South, at the boundary zone between the Ethiopian Rift and Afar in May 2000, in the Ayelu-Amoissa volcanic complex (Keir et al., 2011).

Remote sensing analysis of the 2017-2019 Erta'ale volcanic crisis and InSAR inversion testifies to the continuous magmatic activity within the volcano and underneath, in the rift crust, between 2014 and 2019. This volcanic crisis included the emplacement of three well-characterised dykes along the rift during the period 2014-2017 (Moore et al., 2019).

We report on a hydrothermal fissure, the Yellow Lake Fissure (YLF), located in Lake Asale only 2 km east of the Black Mountain dyke and nearly parallel to it and the NNW Danakil depression trend. It is also parallel to the Dabbahu-Manda Hararo dykes and rift segment.

Most of the recent geologic work at the western border of the Danakil depression near Dallol has been conducted for potash mining. Seismic profiles were obtained and holes were drilled by the mining companies operating on Dallol and in its vicinity. Most data have been acquired on the western side of the Danakil depression, along the margin with the uplifted continental basement. South of Dallol, seismic profiles have been obtained by Allana Potash parallel and perpendicular to the Danakil depression. North of Dallol, profiles have been obtained by Circum Minerals and Yara Dallol. More than 300 holes were drilled by Parsons in the 60's (Holwerda and Hutchinson, 1968), and were complemented by 88 holes by Allana Potash and Nova Potash (Rauche and van der Klauw, 2015). Data and analysis of many drill holes, as well as Allana seismic profiles, have been disclosed by Rauche and van der Klauwe (2011, 2015), and combined with additional data, were used to infer geodynamic interpretations (Bastow et al., 2018). Salts occupy the upper hundreds of meters at least, and probably more than 2 km, of the rift, with increasing thickness from the western margin eastwards. The lower part of the sequence, when attained by the drill holes, includes the Lower Rock Salt, and the upper part, the Upper Rock Salt. In between, an intermediate member, the Houston Formation, includes several tens of meters of potash layers and a distinct halite and anhydrite level disconformable with the Upper Rock Salt formation (Holwerda and Hutchinson, 1968; Rauche and van der Klauw, 2015). The lowermost part of the sedimentary pile, rarely attained in the drill holes, shows clays and conglomerates. The whole sequence has been ascribed a Pleistocene age (Holwerda and Hutchinson, 1968).

Due to seasonal flooding in response to streams coming from the neighbouring highlands, and in agreement with the field observation that the water table is in general not farther than a few centimetres below the surface, Lake Asale can be considered as permanently saturated (Talbot, 2008). Groundwater circulation has been investigated by Anderson and Goode (2017), who highlighted the supply of fresh water from the neighbouring mountains in the West in the shallow subsurface, and brackish and salty waters at greater depth, which is thought to be responsible for karstification of the Upper Rock Salt. Flooding of the salt plain surface generates salt redeposition in the form of a widespread thin layer of white salt crystals. Heating of the sediments by underlying magmatic activity has been interpreted to generate vigorous halokinetic movements within the whole sedimentary pile (Talbot, 1978), leading to solid-state convection (Talbot, 2008; Anderson and Goode, 2017). Such patterns are yet to be reconciled with the apparently undisturbed Houston Formation sampled in the drill holes and the seismic profiles.

The nature of the rift floor underneath the Danakil rift, continental or oceanic, remains unclear, remaining unattained by the drill holes. Late-stage continental stretching prior to oceanisation appears to be the dominant view. Magmatic intrusions do exist in the rift, with the 2004 Black Mountain dyke intrusion in the rift, as well as boulders of basaltic composition in salt dykes in the Dallol dome (Holwerda and Hutchinson, 1968), but are scarce. Noting in addition that the crust is thinner than in other areas in Afar, Bastow et al. (2018) conclude that rifting has not been significantly magma-assisted. There is, however, no direct evidence that the crust below the Danakil rift is continental, and the existence of an oceanic basement cannot be formally dismissed.

In this study, we map and describe the YLF, which has never been formally studied previously. We date the formation and associated hydrothermal activity using satellite imagery, and discuss its significance for the Danakil depression and the Red Sea.

2. Methods

2.1. Field work

The YLF was studied during a 5-day visit to the Danakil rift between 21 and 25 January, 2018, within the framework of the Europlanet 2020 Research Infrastructure Transnational Access activities. A complementary 11-day visit between 12 and 22 January, 2019 made it possible to confirm these observations and gain insight into the evolution of the fissure after 12 months. We named the fissure after a lake located next to the central part of it, also known as Oily Lake or (improperly, according to Afar people) Gaet'ale, which is known for CO_2 emissions (Master, 2016) and its exceptionally high dissolved salt content (Pérez and Chebude, 2017).

2.2. Water geochemistry

Fluids were collected at 2 hydrothermal pools and Yellow Lake. The samples were collected by completely submersing autoclaved sterile glass tubes. After sampling, the glass tubes were hermetically closed with a thick rubber sealing septum. To prevent unwanted leaking or external contamination even more, the flasks were extra firmly sealed by forcibly crimping of an aluminium closure ring on top of the septum. After transport towards the laboratory, the samples were treated and chemically analysed.

2.3. Remote sensing

The remote sensing dataset used and discussed in this paper are given in Supplementary Material 1. High-resolution imagery: KeyHole-4B, OrbView-3, Pleiades-1A/B, QuickBird-2, Spot-6, and WorldView-2 are used to map the details of the YLF and associated features at irregular time steps.

Although all the high-resolution archive imagery available since 1965 was used for this study, only the most significant images are analysed here. The benefits of 10-30 m resolution data: ASTER, Landsat-7, lie in their spectral capabilities, making identification of potential surface composition variations between two consecutive passes, usually not more than 1 or 2 months. They are used to determine the succession of events at the time of YLF formation, in 2004-2005 (Supplementary Material 2). Furthermore, the thermal channels of ASTER are useful to identify possible surface temperature variations associated with the hydrothermal activity of the YLF, both diurnal, and between different orbits. Sentinel 2A/B data were also analysed, but did not yield information not already available using data from the other multispectral satellites? They are not referred to later in this work.

The YLF is nearly fully covered by four 1x1 km pixels from the MODIS Land Surface Temperature dataset (Supplementary Material 3). In spite of this coarse resolution, surface temperatures are measured daily, during daytime and nighttime, making it possible to monitor whether or not development of the YLF in 2004-2005 was associated with significant thermal anomalies at surface.

3. Yellow Lake Fissure: a description

Holwerda and Hutchinson (1968) show an air photograph of the whole Dallol area, including the Yellow Lake area, the resolution of the printed version of which is too coarse to identify any fissure. Unlike many recent fissures in volcanic environments, the YLF does not display any fresh structural features such as tension fractures or normal faults; however, its opening, with no visible vertical block displacement, makes it a probable mode-I crack system. One of the segments, photographed in 2012, is displayed on Figure 10 in Franzson et al. (2015) and described as a tectonic fracture. That figure, like the field photographs displayed here (Figures 4 and 9), illustrates the erosional nature of the crack morphology. The YLF is included in the geologic map discussed by López-García et al. (2020).

3.1. Structural description

The most accurate structural geometry, obtained a short time after fissure initiation, reveals a rich segmentation, from which 7 main zones can be identified (Figure 3). In addition, a 200 m long double segment is hydrothermally active west of the main fissure system and north of Yellow Lake. At segment 1, the YLF broadens to three parallel parts, and intersects a poorly expressed, NW-SE structural trend of unknown origin.

3.2. Geomorphology

Although fissure geomorphology is not spectacular, it has a remarkable diversity of features. Each segment has a dominant geomorphologic expression, which may vary with time (some major changes were noted between January 2018 and January 2019) but several geomorphologic types are found in most segments. They are also observed in the northern YLF area, where the N-S YLF network crosses a NW-SE fracture system, resulting in diffuse hydrothermal activity.

Pools

Some fissure segments are open and partly filled with hydrothermal fluids, sometimes characterised by ascending gas bubbles (Figure 4). These pools are usually less than 1 m long, but a few of them are a few meters long. Franzson et al. (2015) show that in 2012 water was present in at least one much longer fissure portion. A 1.50 m long rod fully penetrated the water of the largest pool found in 2018 and 2019 (Yellow Pool, Figure 3) and did not meet the bottom of the open part of the fissure. Like at

Yellow Lake (e.g., Masters, 2016), dead birds are sometimes observed on the margin of the pools, indicating sufficient CO_2 emissions to suffocate them.

Ridge features

The surface of Lake Asale in the YLF area is made of polygonal salt plates several centimetres thick. This morphologic pattern is also found in other places on Earth. In particular, Jackson et al. (1990) describe similar salt polygons (*namak sefid*) separated by upwelling salts in the Great Kavir, Iran. Along YLF segments, upflows bring clays to the surface at plate edges along a broken line, where they form clay ridges (Figure 5a, 5c), termed "dry mud dykes" in Great Kavir by Jackson et al. (1990). In other areas, the salt plates are sharply broken and tilted, forming triangular-shaped, tepee-like (Talbot, 2008) fractured landforms (Figure 5b). Clay ridges and the rotated and fractured plates are sometimes associated (Figure 5d) in a way that suggests causal relationships.

Jackson et al. (1990, p. 9) mention the occurrence of *kaseh* in Great Kavir, which are probably similar features, forming sharp-edged salt plate pinnacles up to 1 m high, interpreted to form when radiant heat from the sun passing through the salt is absorbed by an underlying dark salt mud, which expands thermally and oozes upward through the salt plate cracks. This mechanism probably applies here too to some extent, with a mud level observed just below the salt plates. However, the usual alignment of this morphology with the YLF suggests that here, some subsurface control is necessary to explain the observed morphology. In Lake Asale, heat of magmatic origin and mud advection might contribute to clay ridge formation and plate desiccation as well.

Other salt plate modifications

Other surface manifestations of hydrothermal activity are less spectacular, occurring with the salt plates or at the boundary between plates. These features are mostly north of Yellow Lake, in the area that was overflowed in 2005 (Figure 3). They are also observed along the YLF, although much less frequently. Figure 6 provides examples of the common morphological features, which may combine and form complex features. Instead of forming ridges, clays expanding at the junction between three plates appear to accumulate as diapiric structures (Figure 6a). Some plates show a circular hole surrounded by a halo of halite crystals (Figure 6b), and sometimes small-scale radiating contractional structures (Figure 6c). Contraction suggests that hole formation might have been accompanied by uplift, after which subsidence and hole shrinkage occurred. Holes are sometimes used as nucleation points for fractures (Figure 6d), or as exit points of sediment accumulating around them from surge deposits (Figure 6e). White and fragile, salt-encrusted bubbles with diameters up to a few centimetres in diameter are sometimes observed to condensate above the holes (Figure 6e). Instead of holes, broader craters with elevated rims may form (Figure 6f). Salt plates may be perforated by aligned holes, perhaps a preliminary to the development of new fractures that subdivide a polygonal plate to a number of smaller polygons typically bounded by a salt recrystallization margin (Figure 6g). Resurfacing by dark clays can sometimes affect an entire polygonal plate (Figure 6h).

In many instances, the YLF is observed as an alignment of polygons which are broader than normally, some of which affected by venting through small chimney fields (Figure 7a). Frequently, bubbling is heard coming from the chimneys. There are no open holes underneath in which bubbles would be seen; and the precise location of the heard bubbles remains unidentified. Venting is sometime associated with platy dark clay resurfacing (Figure 7b). Rarely, these larger polygons are soft and sticky (Figure 7c), and are associated with small brown mud resurfacing patches (Figure 7d). Radial fracturing along the margins of these mud patches suggests that mud emplacement exerts some traction at the surface. Settings like in Figures 7c-d are also favourable to development of salt bubbles.

3.3. Segment characterisation

Segments 1 and 2

Segments 1 and 2 show most of the pools observed along the fissure (Figure 4). The area is however structurally more complex, because it meets another, NW-SE oriented fracture zone of similar type. The surface is either composed of white salt or red salt (Figure 8a, 9a), with the red salt forming a frequently soft and sticky broad continuous patch in the northernmost area. In its northwestern part, approaching the Dallol dome, the red salt is associated with native sulphur deposited in interplate fractures (Figure 8a-b). In some places, a vigorously bubbling salty lake collects near-surface water (Figure 8a). The northern part of Segment 1 is filled with white salt within the broad red patchy area. These segments are the most hydrothermally active of the YLF.

Segment 3

Segment 3 is divided into a western and an eastern part. The western part is exposed as broad salt plates pierced by many small chimneys (Figure 7a). The eastern part is mainly visible as linear brown clay ridges such as those found on Segment 4 (Figure 5a).

Segments 4 and 5

These segments are mainly marked by broad flat plates pierced by chimneys. The northern part of Segment 4, however, is observed as linear clay ridges (Figure 5a). The transition zone between these segments is marked by broad, circular salt plates (Figure 9b). Close to the relay zone linking the segments 4 and 5, Segment 5 displays a few small pools in which salt brines may simply show the shallow groundwater level (Figure 9c). Such pools are restricted to this relay area between segments 4 and 5, in contrary to chimneys, which testify to active subsurface processes distributed over the whole length of these segments. Pool location in the relay zone may denote relay zone fracturing structural control; nevertheless, most pools in the YLF are not observed in relay zones, indicating that relay zone fracturing does not pay a critical role in their development.

Segments 6 and 7

These segments are interacting *en échelon* fractures. They are marked on the ground by coalescence of linear 5-10 cm high ridges at the edge of the salt plates located above the fissure, as well as by periodically spaced red circular patches 1 or 2 m in diameter due to native sulphur crystallisation (Figure 9d-e). The relay zone between the two segments shows native sulphur crystallisation on the white salt plates, as well as a few salt bubbles (Figure 9f-g).

3.4. Composition and properties of fluids

Water temperature, pH, composition and mineral content of two pools were analysed, and compared to with similar measurements at Yellow Lake (Table 1). Temperature was found to be slightly less than ambient air day temperature (~40°C, Supplementary Material 3), and pH moderately acidic. Holwerda and Hutchinson (1968) suggest that the gas in the bubbles of a large brine pool, presumably Yellow Lake, is CO_2. Because temperature is well below the boiling point, both from measurements and ASTER surface temperatures (Section 4), bubbling is interpreted as consequence of depressurisation of CO_2, perhaps under supercritical conditions (Span and Wagner, 1996) at depth in relation to magmatic processes. Brine resurfacing on the Dallol dome itself indicates isotopic exchange with mafic rocks at depth (Gonfiantini et al., 1973). Water composition is close but not similar in the two pools, nor is it identical with the composition of Yellow Lake, suggesting that the fluid source is the same, but its history before reaching the surface differs at the three sites. The identified minerals include halides and chlorides. While most halides and chlorides

are found in many possible environments, chloromagnesite is a very rare mineral identified in melt inclusions in unaltered olivines in kimberlites (Golovin et al., 2003) and peridotites (Sharygin et al., 2013). Like at Yellow Lake, chloromagnesite is found with halite and sylvite at fumaroles on Mount Vesuvius (Pelloux, 1927). Finding it in the Yellow Lake may testify to connection with an ultramafic body underneath. Tachyhydrite is another rare mineral because of its tendency to deliquescence. Its detection n Yellow Lake and in the Yellow Pool is made possible by the very high Ca^{2+} concentration. Moors et al. (2020) discuss more results, obtained from various water bodies in the Dallol dome area.

4. Initiation of the Yellow Lake Fissure

YLF initiation and evolution can be inferred from the analysis of remote sensing data. Fracturing along the northern segments is apparent in 1965 (Figure 10a, see also Supplementary Material 4 for the uninterpreted satellite images shown on Figure 10), in the form of lineaments which are still observed in 2003 and appear to be at least in part related to Yellow Lake overflow (Figure 10b). However, only on December 17th, 2005 is the YLF observed (Figure 10c).

Since 1965, the dominant observed fracture trend is NW-SE to NNW-SSE (Figure 11). However, in 2003, N117E is the dominant visual trend at the scale of the whole area, and most fracture trends are in the sector NW-SE to N-S. The YLF trend itself, N165E, is visible (green on Figure 11) but does not dominate the statistics (Figure 11b). The YLF itself is absent. In 1965, the YLF trend is clearly dominant, but similarly, is not developed as an entity (Figure 11a). The YLF is first clearly seen at high (meter-scale) resolution on December 17th, 2005. The strike frequency and length distribution by 10° bins show strike variations between N-S and NW-SE (Figure 11c), reflecting the detailed geometry of the fracture network, which includes relay zones and associated propagation features. The N117E trend already noted in 2003 persists, and intersects the northernmost YLF.

The absence of high resolution imagery between June 2003 and December 2005 can be mitigated by time-series analysis of lower resolution imagery during this period in the near-infrared spectral range. Comparison of bands 5 and 7 (30m/pixel) on Landsat-7 images, sharpened by the higher resolution band 8 (15m/pixel), reveals that the composition of the surface changed along the trace of the YLF between October 13th, 2004 and November 14th, 2004 (Figure 12). The fit to the trace shows that the YLF likely formed within this time interval.

Figure 12 shows that the full length of the YLF was achieved before November 14th, 2004. However, the detailed geometry of the segments as seen at the scale of 1m/pixel on December 17th, 2005 (Figure 10c) may have been achieved later. There is no spectral evidence of activity of the YLF between November 14th, 2004 and April 7th, 2005, but narrow resurfacing along the YLF is observed on June 10th, 2005, leaving the possibility of renewal of tectonic activity between April and June (Figure 13). The whole study area was flooded by Lake Karum by late April, preventing more precise dating. Hydrothermal activity has been intense in the Yellow Lake area, however, throughout the year 2005 (Supplementary Material 1 and 2).

InSAR analysis indicates that the volcanic crisis that started at Erta'ale on January 16, 2017 did not affect the topography in the area of the YLF (Xu et al. 2020). Comparison between satellite imagery before and after the main, January 2017 event (20.11.2016: WorldView-2 vs. 12.02.2017, ASTER), confirms that the fissure system remained unaffected at surface.

5. Yellow Lake Fissure and hydrothermal activity

Elliptic red mud patch

The northern YLF area abundantly displays red salt at surface. In addition, red patches forming together a fragmented elliptic feature are observed on satellite images (Figure 10). In spite of frequent resurfacing by waters from Lake Karum, the shore of which is usually located ca. 15 km south of the YLF, and runoff from the neighbouring mountains, these patches have been remarkably stable since at least 1965 (Figure 14). Flooding reveals that these patches are subtle topographic highs (Figure 14b). From observation and oral reports, the water column during the floods does usually not exceed 10-20 cm, and numerous Landsat-7, Landsat-8, and ASTER images show that flooding very rarely attains the top of the patches. A UAV-borne stereotopographic survey was conducted in January 2019, and superimposition of the DTM onto satellite images spanning a 53 years' time interval indeed reveals that the shape of the patches has not significantly changed through time, and their current elevation above the surrounding Danakil depression floor is indeed of the order of 20 cm (Figure 14d).

This elevation difference is quantitatively emphasized on Figure 16 and Figure 17, where a comparison between the average elevation of the main red patches and the average elevation of neighbouring areas also shows the red patch surfaces rising up to a few tens of centimetres. This is observed both when red patch elevation follows the boundaries of 1965 (A-D on Figures 15-16) and when it follows more closely the boundaries of 2019 (E-I). The YLF itself (J-L) is not significantly more elevated than its surroundings.

The red patches are older than any available high-resolution satellite image. A 1962 KeyHole-5 mission image with a resolution of 28 m shows slightly darker pixels in this area, suggesting that the patches were already present in 1962. Mud flows from one or a few local vents are a plausible origin, a hypothesis that might tested analysing existing aerial photographs.

Hydrothermal activity at Yellow Lake and YLF

The fissure itself has been the locus of hydrothermal activity since its formation. Its first appearance on low resolution multispectral imagery on November 14th, 2004 (Landsat-7 bands with 30m/pixel Figure 12 and Supplementary Material 2), in spite of its narrow lateral extent, ~1 m, implies resurfacing and/or alteration around the fissure.

However, hydrothermal activity also proceeded at Yellow Lake. As soon as the YLF was formed, hydrothermal activity occurred north of Yellow Lake. The dark deposits which are visible north of Yellow Lake on Figure 12 correspond to hydrothermal activity between October and November 2004. This activity is clear on the video of Supplementary Material 2, which further shows that activity has resumed in the second half of January 2005, and lasted until early April at least. The area was then fully flooded, with the possible exception of the two highest points of the elliptic red mud patch. There is evidence of continuing hydrothermal activity north of Yellow Lake between July and December 2005.

The situation is more accurately known by mid-December 2005 due to high-resolution imagery (Figures 3 and 10). The dark deposits north of Yellow Lake on Figure 10 are connected to Yellow Lake, suggesting that they were formed at a Yellow Lake overflow event (brown on Figure 3). They are surrounded by light-edged aureoles interpreted as marking the maximum extent of the flooding, and are made of some evaporitic salts that were precipitated when the overflow flood ponds desiccated. It is apparent from the video (Supplementary Material 2) that the lobes include material coming from overflow of along a 300 m long, N-S oriented fissure starting at Yellow Lake, and another, 100 m long NNW-SSE oriented fissure segment a few hundred meters northward (Figure 3). The N-S segment is not apparent as a tectonic entity on any of the satellite images since its formation, whereas the

NNW-SSE segment, mapped on Figure 3, is identified through NNW-SSE trending salt plate edge alignments in 2018 and 2019, and is associated with subsurface bubbling and venting as on Figure 7a.

Yellow Lake is not aligned with the YLF. Analysis of satellite images dating back to the initiation of the YLF indicate that Yellow Lake has its own associated fracture system, developed north of it. Although not directly visible today, Yellow Lake was the locus of the most intense hydrothermal activity when the YLF initiated. Hydrothermal activity along the YLF has been mostly constrained to the fissure itself, with minor overflow limited to the time of fissure initiation.

Pressure-driven, low-temperature hydrothermal flow

Whether magmatic heat was significant in the process of YLF development may be evaluated by the temperature of the fluids at the surface when the fissure open. The temperature of the fluids that were first ejected from the hydrothermal fissure, and led to resurfacing along its trace is investigated using thermal data obtained by ASTER and MODIS (Supplementary Material 3). ASTER surface temperatures are available for 14-11-2004 during daytime, just after YLF initiation. They are also available on 09-01-2005 and 17-02-2005 at nighttime, at the beginning of a hydrothermal crisis centred at Yellow Lake and to a lesser extent, at some fissure segments north of Yellow Lake (see video in Supplementary Material 2). MODIS daily daytime and nighttime temperatures are available at a resolution of 1 km. None of these datasets show evidence of anomalous surface temperatures in this time span, suggesting that the fluids that accompanied YLF opening during fall 2004 and those of the subsequent hydrothermal crisis did not advect significant thermal energy to the surface.

This is similar to the current situation, where the fluids in the bubbling pools located along the YLF as well as Yellow Lake have ambient air temperature (Table 1). Although not measured, the temperature of White Lake, which was the most active bubbling body during the 2019 field visit, was also similar to ambient air, showing that bubbling was pressure-driven. Holwerda and Hutchinson (1968) report that the bubbles in this part of the Danakil depression, such as Yellow Lake and Skating Rink, have a CO_2 composition.

In contrast, near Black Mountain and the Dallol dome, hot springs having temperatures as high as 130°C had been measured in the 1920's (as reported by Holwerda and Hutchinson, 1968, and Talbot, 2008). Bischofite, which loses water at ~120°C and fully melts at ~710°C (Warren, 2016), is frequently erupted at Black Mountain. Black Mountain and the YLF, although at the same close distance to the Dallol dome, are therefore two very different geological manifestations. Black Lake, at the northern tip of Black Mountain, was visited in January 2018, and was found at ambient air temperature. It is therefore in a thermal state similar to Yellow Lake, White Lake and the YLF.

6. Discussion

Coeval Black Mountain dyke emplacement and YLF opening

Emplacement of the Black Mountain dyke and initiation of the YLF is coeval when the resolution of the available data is considered, showing that both are likely related.

Initiation of the YLF between October 13 and November 14, 2004 encompasses the whole period of Black Mountain dyke injection inferred from the seismic record, i.e. October 22–November 4. Independently, InSAR modelling showed that a late stage of dyke intrusion occurred between October 27 and December 1st (Nobile et al., 2012). The InSAR model includes the Black Mountain dyke, and also predicts normal displacement along a blind normal fault located west of the dyke. However, the InSAR model residual is partly consistent with ground displacement along the YLF (Figure 17). This is not surprising, since opening and overflowing of the YLF likely generated

topographic changes of amplitude observable by InSAR. From satellite image monitoring and InSAR altogether, it appears likely that the YLF formed between October 27 and November 14, 2004.

The advocated blind normal fault is parallel to the dyke, but also to the Danakil rift margin, where seismic profiles indeed shows rift-parallel border faults (Rauche and van der Klauw, 2915; Bastow et al., 2018). Its existence and activity coeval with dyke emplacement is however not confirmed by independent data. Moreover, it is also parallel to the YLF, suggesting that accounting for YLF opening in addition to dyke emplacement in an InSAR model would perhaps make necessary modification of the blind normal fault parameters, or even question its existence and displacement. InSAR data reprocessing taking YLF opening into account in addition to dyke opening would help clarify this point.

Conventional dyke emplacement models, however, hardly explain the development of a vertical tensile fracture propagating at the surface in response to emplacement of a thin (~1 m) dyke at a depth of 2-6 km (Nobile et al., 2012) located at a horizontal distance as far as 2.5 km. For instance, pioneer experimental models by Mastin and Pollard (1988) predict normal faulting at this distance, whereas the results obtained by Abdelmalak et al. (2012), Wyrick et al. (2015) and Poppe et al. (2020) would rather suggest thrust or reverse faulting. If fracture toughness is large enough, no deformation is expected (Lister, 1990; Roper and Lister, 2007).

Additionally, understanding YLF initiation needs hydrothermal activity to be taken into account. Opening of the YLF in 2004 occurred while hydrothermal activity in the area was ongoing for many years. In the next section an attempt is made to first understand the origin of hydrothermal activity, then YLF initiation in this context.

Hydrothermal activity in the YLF area in response to a secondary Dallol sill

We note that the elliptic red patch, interpreted as a hydrothermal mud flow, exists for several decades. Yellow Lake exists since the mid 60's at least (Figure 10a). Yellow Lake has also been reported bubbling in the receding works, testifying to permanently pressurised groundwater underneath. White Lake, the largest water body in the YLF area, was vigorously bubbling during the 2019 field campaign, and KeyHole imagery indicates that it is a long-lasting lake as well, developed from the merging of two smaller lakes visible in 1965 (Figure 10). In fact, evidence of groundwater release, and therefore pressurisation underneath, exists at these sites for as long as data are available. It requires magmatic heat at depth much before the 2004 Black Mountain dyke intruded the crust. The ambient hydrothermal fluid temperatures measured at surface places constraints on the distance between the surface and the depth of the magma body, and its level of cooling since emplacement.

Warren (2015) describes how the Dallol dome may have been uplifted in response to dyke intrusion piercing the Lower Rock Salt, and dyke bifurcation toward sill at the level of the Potash Beds in the Houston Formation. Sill propagation from dyke in heterogeneous rock layers and variable pore pressure conditions is mechanically well understood (e.g., Gressier et al., 2010). The specific rheology of salts, especially hydrated salts, makes this evolution easier (e.g., Schofield et al., 2014). The Houston Formation offers a range of hydrated mineral-rich layers (mainly, from bottom to top, kainite, carnallite, bischofite, and carnallite; Rauche and van der Klauw, 2011, updated in Rauche van der Klauw, 2013), the mechanical strength of which is small and easily further decreased by decomposition and melting at low temperature. The melting temperature of carnallite and bischofite, 110-120°C (Warren, 2016), may allow them to melt ahead of a propagating intrusion even before their contact, depending on the combination of reaction kinetics, ambient thermal diffusivity, and intrusion propagation speed. The resulting brines recrystallise further away around the intrusion

as new, more competent, anhydrous or less hydrated minerals (Schofield et al., 2014). The hydrous mineralogy of the Houston formation is capped with layers rich exclusively composed of anhydrous minerals (halite, anhydrite, and sylvite; Rauche and van der Klauw, 2011).

If the Dallol dome indeed uplifted in response to sill intrusion, the sill (hereafter called the Dallol sill) should be of exceptional dimensions in order to uplift Dallol by several tens of metres. Due to this size, one would expect a complex intrusion geometry; in particular, the Dallol sill may have extended to adjacent areas as thinner, secondary magma sheets connected to the main intrusion. López-García et al. (2020) argue that the Dallol sill was injected "later than 600 years ago", and is still hot. It would have propagated far enough toward Yellow Lake to continue nowadays to pressurise groundwater in the area of Yellow Lake, fed by brines generated between the sill and the surface. Exploratory holes have never been drilled in the YLF area, which is outside the potash exploration concessions, leaving the sill interpretation unproven by direct evidence. The closest hole is located 1.5 km east of the YLF segment 6, with 10 additional holes along the YLF trend further south (Figure 18). None of these distant holes have met any magma intrusion (e.g., Rauche and van der Klauw, 2013), nor there is any evidence of mineralogical transformation of the original Houston Formation mineralogy to less hydrated or anhydrous minerals following the mineralogical transformation reactions detailed in Rauche and van der Klauw (2011) and Warren (2015). As a consequence, the existence of the Dallol sill, perhaps ramifying to secondary sills farther away, is plausible but keeps undemonstrated from subsurface data.

Although conceptually simple, sill propagation at the Potash Beds level of the Houston Formation may be more complex because the Potash Beds are not flat. Correlating their depth south of the Dallol dome from the drilling cores, Rauche and van der Klauw (2013, Enclosure B) map a deformed rift-trending syncline in which the Marker Beds, the topmost level of the Houston Formation, are found 100 m below the surface on the western side of the rift. The Marker Beds attain the maximum depth of 700 m south of the Dallol dome. They are found at 275 m below the surface 1.5 km east of YLF Segment 6 (Figure 18). Sills are classically defined as horizontal intrusions, ideally propagating perpendicular to the lithostatic pressure assumed vertical. Due to the inclination of the Potash Beds, any sill propagating at this level would need to be inclined as well, or to cross lithologic boundaries with more competent layers. From the core data (Rauche and van der Klauw, 2013, Enclosure B), the maximum sill inclination would need to be in the order of 10 degrees to perfectly follow the Potash Beds. Such a structural control of sill emplacement by stratification in addition to the ambient stress field is not uncommon; for instance, it is thought to have been significant in dyke swarm emplacement in western Ethiopia (Mège and Korme, 2004, structural data complemented by magnetic foliation imbrications at dyke margins, Schultz et al., 2008).

Rauche and van der Klauw (2015) extrapolate the depth of the Marker Beds to 350-400 m south of Yellow Lake. This depth is loosely constrained; nevertheless the general pattern is that the Potash Beds are likely shallower at Yellow Lake and the southern YLF than in any other place of Lake Karum at the same distance to Dallol in areas where drilling cores are available. If the depth of the Potash Beds in the YLF area is shallow indeed, and if they were indeed intruded by an extension of the Dallol sill, then the close proximity of the sill to the surface may be a reason for the pressurised groundwater above it to be more easily expressed at the surface than for instance, above the 2004 dyke, where the Marker Beds are twice deeper (Figure 18).

Holwerda and Hutchinson (1968) mention the existence of rare altered basalt fragments in salt dykes on the Dallol dome. During the 2019 campaign, a search for basaltic fragments on the western side the Dallol mound yielded a fresh fallen dolerite sample next to one of the salt dyke (Figure 19). This

sample confirms the presence of a shallow mafic body crystallised at shallow depth under the Dallol dome, which could be the hypothesized Dallol sill.

Opening the YLF in response to sill propagation from the 2004 Black Mountain dyke

YLF cracking is found in this work to have initiated during fall 2004, much later than the hydrothermal activity in the area. It is therefore possible that the pools located along the fissure segments generated in 2004 and 2005 tapped into the groundwater reservoir already feeding Yellow Lake and White Lake. The composition of Yellow Lake and two pools located along the YLF (Table 1) is broadly similar, with slight differences that may be attributed to local heterogeneities in the salt layers along the fluid flow paths.

The question remains how to connect the coeval formation of the YLF and the remote Black Mountain dyke. Given the distance between both features, and the very favourable lithological conditions of sill propagation from a dyke in the Danakil depression (as pointed out in the section above), it can be suggested that similar to the emplacement of the Dallol sill, the Black Mountain dyke may have given birth to a sill. Similarly, this sill needs to be shallow enough to pressurise groundwater, but deep enough for heat not to be significantly advected toward the surface. A major difference between the Dallol sill and the putative Black Mountain sill is that the former must have been voluminous enough to generate exceptional surface uplift, in the order of 30 m, whereas the Black Mountain sill, fed by a dyke estimated to be ~1 m thick only (Nobile et al., 2012) at a depth of hundreds of metres, has little chance to generate any surface deformation. In both cases, sill propagation is favoured at the Potash Beds, the weakest level of the sedimentary pile.

Although the focal mechanisms of the earthquakes of the seismic swarm that accompanied dyke propagation in 2004 could not be determined (Nobile et al., 2012), such information might not have been conclusive about dyke transformation to sill, because the low strength level in which the sill is expected to propagate would result in aseismic propagation.

The putative Black Mountain sill may have triggered the opening of the YLF due to the convergence of several factors.

1. We note that the whole crust is in extensional regime, being at an extensional plate boundary. As a consequence, crustal dilation at depth needs to be balanced by tectonic stretching at shallower depth and the surface. This simple view has long been established, based on field observations, in the similar geodynamic setting of the rift zone of southwest Iceland (Forslund and Gudmundsson, 1991). The YLF would therefore release the tensional stress at the plate boundary, released deeper by dyke dilation.

2. Sill propagation locally modifies the balance of the principal stresses. Due to sill propagation, the deviatoric stress may have been locally increased enough to result in salt pile fracturing. The YLF would have initiated at a site where the salt pile was closest to rupture ahead of the propagating sill.

3. Groundwater pressurisation probably helped in increasing the deviator. The location of the YLF would have therefore been determined by the distribution of groundwater pressure, and initiated where it is the highest. By observation, this zone of highest pressure is defined in map view by the Yellow Lake – White Lake – Red elliptic mud patch line, and in a vertical section, above the thin sedimentary pile above the sill, at 350-400 m (Figure 18).

4. The Black Mountain sill may have propagated along the Potash Beds, similar to the Dallol sill; however, if the secondary Dallol sill propagated until Yellow Lake is still cooling, the Dallol sill itself may also have been a preferential level of magma propagation, resulting in a composite sill (e.g.,

Wada, 1992). The Black Mountain dyke would have therefore been trapped by the Houston formation at a depth > 700 m (Figure 18) and risen eastward following the cooling secondary Dallol sill to the Yellow Lake/YLF area.

The formation of the YLF from the propagation of a sill from the Black Mountain dyke may therefore be explained using the existing observations and measurements, interpreted using simple mechanical considerations.

7. Conclusion

This work provides the first description and analysis of a 15 years old fissure system located in northern Afar at the boundary between the Nubian plate and the Danakil microplate. We named this fissure system the Yellow Lake Fissure. We mapped and characterised the geologic activity of the fissure system, emphasizing the diversity of its surface morphology. Using spaceborne data, we showed that its initiation was coeval with emplacement of the Black Mountain dyke (a name given to the dyke that intruded the crust below Lake Karum in 2004). The long distance between the dyke and the fissure system makes direct causal relationships unlikely; the problem to be solved is that of strain transfer from the lower sedimentary pile, in which dyke dilation releases the stress accumulated at this plate boundary, to the upper sedimentary pile, where much farther, the Yellow Lake Fissure system releases plate boundary stress through tension fracturing. To constrain the solution, we used geology and topography data collected during field work, data from spaceborne thermal sensors, and from the nearby potash drilling holes. Some simple mechanical considerations make it possible to propose a hypothesis of Yellow Lake Fissure initiation from a sill propagating from the Black Mountain dyke. Like the much larger Dallol sill, the Black Mountain sill may have propagated within the Houston Formation. The latter may actually be the only level within the sedimentary pile where magma propagation is favourable due to its highly hydrated mineralogy. Slowly rising east, the sill would have met the Yellow Lake area, where very active hydrothermal circulation has long taken place. Sill penetration in this overpressurized portion of the salt pile would have increased the deviatoric stress to rupture, initiating the Yellow Lake Fissure. Residual stress was released along the fissure a few months later.

The Yellow Lake Fissure is in the axis of the Red Sea oceanic spreading centre, which enters the northern Afar in the Gulf of Zula. Although modest in length, a few kilometres, it appears to be the only basin fissure of northern Afar currently active the dynamics of which may be directly related to Red Sea spreading. It uniquely testifies to the magmatic, tectonic, and hydrothermal processes that a continental rift is subjected to in its latest evolution stage before oceanisation. In this paper we proposed ideas to understand this ultimate step better. Rather than being conclusive, we hope that the observations and ideas developed will attract enough interest to trigger new investigations that will finally connect this last step to the first oceanic spreading steps. We foresee that this connection can be established by following the Danakil depression northward, from the Yellow Lake Fissure to the Gulf of Zula.

Table

Table 1 – Location of the sampling sites and properties of the sampled fluids. Yellow Pool and Red Pool are located along Segment 1 of the YLF.

	Yellow Pool	Red Pool	Yellow Lake
Latitude	14.2279°N	14.2282°N	14.2134°N

Longitude	40.3189°E	40.3184°E	40.3214°E
T (°C)	32.0	35.1	41.2
pH	3.7	3.5	3.4
Conductivity ($mS.cm^{-1}$)	395	494	598
Minerals	Halite Tachyhydrite	Sylvite Carnallite	Halite, Sylvite Tachyhydrite Chloromagnesite
Dominant cations (based on mass %)	Ca^{2+}>Na^{+}>Mg^{2+}>K^{+}	Ca^{2+}>Mg^{2+}> K^{+}>Na^{+}	Ca^{2+}>Mg^{2+}>Na^{+}>K^{+}

pH and conductivity is measured in lab at 25°C. López-García et al. (2020) additionally identified carnallite at Yellow Lake.

Figure captions

Figure 1. Geologic setting of the study area, located at the southern edge of the Dallol dome. The oceanic rift structures are shown in blue (propagation direction given by the blue arrow, after Hughes et al., 1991; Bosworth et al., 2005), and the East African Rift main normal faults in red (latest propagation direction in red; Wolfenden et al., 2004). The Red Sea rift segment onshore is shown in black, and the black box locates Figure 2a. The main faults of the Tertiary Somalia grabens and coeval Ogaden dyke swarm trend, are shown in grey (Leroy et al., 2012; Mège et al., 2015). The extent of the Oligocene flood basalts is after Mège et al. (2015). The brown arrows indicate plate kinematics. Green lines locate the main thrust faults from the Makran accretionary wedge.

Figure 2. Tectonic context of the Yellow Lake Fissure. The background image is from WorldView-2, 20-11-2016. The IDs of the images used in this work are given in Supplementary Material 1.

Figure 3. Yellow Lake Fissure structural map. Red salt outcrop boundaries are mapped after Pleiades image, 2017-10-21. Yellow Lake overflow and the extent of the resurfacing lobe in the Yellow Lake area are mapped from their original extent visible on OrbView-3 image (1 m/pixel), 2005-12-17. Fissure resurfacing in the northern area is tracked from 2005 but is mapped from Pleiades (0.5 m/pixel), 2012-11-15. The surface area of Yellow Lake is taken at its maximum extent (4200 m^2), measured on a QuickBird image (0.33 m/pixel), 2003-06-02. Historic pool data are from the images mentioned above, plus other data from Pleiades (0.5 m/pixel) and Spot-6 (1.5 m/pixel) distributed between 2012 and 2019. Native sulphur deposition mostly occurs in circular patches, which are here usually mapped as patch fields representative of the exposures in the period 2018-2019. Chimney fields, active and dry pools, and bubbling areas refer to observations made in January 2018 and 2019. The fissures are a synthesis of observations on all the satellite images mentioned above. White Lake is observed as a single body in 2003, but as two smaller lakes in the earlier high resolution imagery (1972, KeyHole-4B, 2 m/pixel, 1965, KeyHole-4A, 2.8 m/pixel).

Figure 4. Typical morphologies of Yellow Lake Fissure along segments 1, north of Yellow Lake. Similar fissure morphology is observed along Segment 2. (a) Salt-covered fissure (segment 2 on Figure 3). The fissure locally splits into two parallel fissures, which then merge and hosts a pool in the background; (b) the northern segments display hydrothermal pools oriented along the fissure. This view shows Yellow Pool (Table 1), the largest pool identified in 2018-2019, also visible in the background in (a). The hydrothermal fluids are slightly bubbling at the end of the pool; (c) oiliness of the hydrothermal fluid in one of the pools. Oiliness is due to the huge amount of dissolved salts; (d) some pools are heavily bubbling, like Red Pool (Table 1), showed here, whereas some others, not always more distant than 10-20 meters, are not bubbling at all. Photographs taken in January 2018.

Figure 5. Linear landforms along the YLF. (a) Clay ridges in segment 2, which on satellite imagery can be mistaken for fresh open cracks; (b) Triangular-shaped, vertically inclined fractured salt polygons forming linear ridges in segment 3; (c) close view of a clay ridge in segment 3; (d) mixed clay and triangularly fractured plate morphology. (a) to (c) were photographed in January 2018. (d) was photographed in January 2019.

Figure 6. Salt plate morphologies associated with subdued parts of YLF segments, part 1. (a) Expanded clays at the junction between three plates; (b) circular holes with surrounding welded salt crystals; (c) circular holes with halo and contractional microridges; (d) circular hole with associated fracture nucleation; (e) circular holes showing evidence of surges and halite recrystallization; a fragile white bubble with a thin salt crust is seen on the upper left; (f) cratered plate; (g) plate internal fracturing and fracture edge recrystallization of halite. On the left, plate edge geometry indicates probable formation by coalescence and enlargement of circular holes (dense circular hole alignments are indeed observed in some plates); (h) full dark clay platy resurfacing and spreading on salt plates. The photographs were taken in January 2018.

Figure 7. Salt plate morphologies associated with subdued parts of YLF segments, part 2. (a) Salt venting field along large YLF polygonal plates; (b) close view of a vent associated with platy dark mud resurfacing; (c) Large soft and sticky fractured polygonal plate along the YLF; (d) perhaps focusing on densely fractured zones along such plates, dark mud upflows emerge at surface. The radial patterns along the dark mud suggests forceful mud spreading at surface. Photographed in January 2018.

Figure 8. Small-scale morphology of the area of segment 1. (a) Vigorously bubbling lake (White Lake on Figure 3). The presence of bubbles, presumably of CO_2 composition, indicates results from degassing, whereas the many small streams converging toward the lake collects shallow surface water; (b, c) Native sulphur deposition along plate edges. Photographs taken in January 2019.

Figure 9. Characteristic linear features of some segments. (a) View of one of the northernmost part of Segment 1, viewed to the South; (b) Relay zone between two échelon fissure segments in Segment 4, view toward South (14°12'47.73N, 40°19'24.9"E). Note the many small chimneys piercing the plates, as in Figure 7a; (c) View to the South of Segment 5 next to the relay zone with Segment 4, showing small chimneys and salt brine pools (14°12'46.87"N, 40°19'25.36"E); (d) View of Segment 6 toward south (14°11'50"N, 40°19'.67"E); (e) View of segment 7 toward north (14°11'47.62"N, 40°19'48.22"E). Photographs taken in January 2019. The triangles indicate the end of segments. (f) View of the relay zone between segments – and 7 toward East. (g) Closer view on the relay zone area, showing native sulphur and salt bubbles. Photographs taken in January 2019.

Figure 10. Structural evolution of the Yellow Lake Fissure area since 1965. The black lines are fracture lines either exposed to the surface, along which pools are sometimes located, or linear salt plate edge alignments suggestive of deeper tension fracturing or fracturing at subcritical stress. YL stands for Yellow Lake. Left: fracturing already observed in 1965 by KeyHole 4-A (2.4m/pixel, image ID); middle: additional fracturing observed in 2003 by Quickbird-2 multispectral (2m/pixel; Gram-Schmidt pansharpened to 0.5 m/pixel); right: fracturing observed since the first post-YLF high-resolution satellite image, by OrbView-3 (1m/pixel), in 2005.

Figure 11. Strike analysis for the fractures observed in 1965, the additional fractures observed in 2003, and the fractures observed since 2005 (Figure 10). In the absence of any observed kinematic indicator that would testify to shearing, all the fractures are considered tensile. The upper plots report show the frequency of individual fractures. The lower plots show the cumulated frequency of fracture lengths, which better represents the dominant expressed deformation strikes. The green and blue sectors correspond to the mean YLF trend (N167E) and NW-Se fracture trend (N117E),

respectively. Analysis conducted using SG2PS (Sasvári and Baharev, 2014). Uninterpreted satellite images are provided in Supplementary Material 4.

Figure 12. Surface change along the YLF trace during fall 2004. The image is a composite colour of Landsat-7 images obtained November 14th, 2004 and October 13th, 2004. The red, green and blue channels are the difference between bands 5 (1.650 µm, 30 m/pixel), 7 (2.220 µm, 30m/pixel), and 8 (panchromatic, 15m/pixel), respectively, Gaussian-stretched. The YLF structures observed since December 17th, 2005 (Orbview-3) are superimposed (b) onto the image composite (a).

Figure 13. Surface change along the YLF trace during winter and spring 2005. The YLF is not much apparent in February and March, in contrary to June, where the YLF trace is well delineated and suggests renewed tectonic activity. Note the intense hydrothermal activity focused in the Yellow Lake area. More data and the image IDs are presented in Supplementary Material 1 and 2.

Figure 14. Evolution of the red salt patches through time. (a) The oldest image shows them already formed. Corona-4A image, 2.4m/pixel. (b) The red patches remain as islands during the October 2001 floods. Landsat-7 colour composite of bands 7 (red), 4 (green), and 2 (blue) of resolution 30m/pixel, with Gram-Schmidt pansharpening with Band 8 at 15m/pixel. (c) Red patch geometry remains unchanged in 2003 (Quickbird-2 image, 2.5m/pixel, with Gram-Schmidt sharpening with panchromatic band at 0.67m/pixel). (c) Similar observation is made in 2019 (Pleiades-1B, 2m/pixel, with Gram-Schmidt sharpening with panchromatic band at 0.5m/pixel). In (a), (c), and (d), UAV-based topography is given with 0.1m-spaced contours. contours of length < 500 m were filtered. Absolute elevation values can be retrieved from Figure 16.

Figure 15. Red patch and YLF-cantered areas in which elevation is averaged on Figure 16, and location of reference areas in salt flat used for as base level for comparison.

Figure 16. Comparison between elevation of red patch areas and YLF, and reference areas in the salt flat. The boundaries of the areas used for topographic averaging are located on Figure 15.

Figure 17. Residual of InSAR deformation model for the period 27-10-2004/01-12-2004, with the location of the YLF and the trace of the non-emergent Black Mountain dyke, modified after Nobile et al. (2012). The Black Mountain dyke is accounted for in the model, and is therefore not expected to be consistent with the deformation remaining in the residual. One fringe, from blue to red, is 2.81 cm.

Figure 18. Depth distribution of the Marker Beds, the uppermost part of the Houston Formation, in metres below the topographic surface. The depth is only constrained by drilling cores (black squares). The contours and drilling sites are from Rauche and van der Klauw (2015, Enclosure B). The location of the YLF and the coeval Black Mountain dyke is given. Note that the depth of the Marker Beds in the YLF area, although loosely constrained, is shallower than along the Black Mountain dyke and most of the drilled basin. The background image is a pansharpened composite of bands 7, 4 and 2 of a Landsat-8 image acquired on 13-01-2018.

Figure 19. Mafic enclaves from a putative Dallol sill. (a) Salt dyke at the bottom of which a dolerite sample was retrieved; (b, c) examples of altered mafic enclaves within this salt dyke, plausibly similar to those noted by Holwerda and Hutchinson (1968); (d) Dolerite sample in the hand of Hanjin Choe, for scale; (e) Sawcut fragment of the sampled dolerite, exhibiting typical plagioclase phenocrysts. Location: 14°14'N, 40°17'E. Photographs: a-d: Daniel Mège; e: courtesy Benjamin van Wyk de Vries.

Supplementary material

Supplementary Material 1 (pdf file). Description of the material used in Supplementary Material 2 (video): Evolution of the YLF area between August 26th, 2004 and December 3rd 2005, and product IDs of the satellite images mentioned in the text.

Supplementary Material 2 (video). Evolution of the YLF area between August 26th, 2004 and December 3rd 2005.

Supplementary Material 3 (pdf file). Surface temperature during YLF formation (2004-2005) from ASTER and MODIS.

Acknowledgements

Field work was funded by Europlanet 2020 RI, and laboratory work by D. Mège by the EXOMHYDR project. Europlanet 2020 RI has received funding from the European Union's Horizon 2020 research and innovation programme under grant agreement No 654208. The EXOMHYDR project is carried out within the TEAM programme of the Foundation for Polish Science co-financed by the European Union under the European Regional Development Fund. The Dallol dolerite sample, collected by Hanjin Choe was retrieved during a most enjoyable field afternoon with Benjamin van Wyk de Vries, Viktor Vereb and Miruts Hagos on the Dallol dome, with logistics kindly organised by Yara Dallol B.V. staff under the direction of Henok Tsegaye. Benjamin van Wyk de Vries prepared the sawcut dolerite fragment shown on Figure 18. Apart from the cited KeyHole-4B data, the high-resolution satellite data used in this work were provided by the European Space Agency under the Restrained Dataset research funding programme. ASTER, Landsat, and OrbView-3 datasets courtesy to the U.S. Geological Survey. The ASTER kinetic temperature data were retrieved between 2020-04-06 and 2020-04-08 from https://lpdaac.usgs.gov, maintained by the NASA EOSDIS Land Processes Distributed Active Archive Center (LP DAAC) at the USGS Earth Resources Observation and Science (EROS) Center, Sioux Falls, South Dakota (https://lpdaac.usgs.gov/products/ast_08v003/).

References

Abdelmalak, M.M., Mourgues, R., Galland, O., and Bureau, D., 2012, Fracture mode analysis and related surface deformation during dyke intrusion: Results from 2D experimental modelling: Earth and Planetary Science Letters, v. 359–360, p. 93–105, doi:10.1016/j.epsl.2012.10.008.

Anderson, M., and Goode, T.C., 2017. Appropriate catchment management can improve the profitability of a mine: a case study from Dallol, Ethiopia. In: Wolkersdorfer, C., Sartz, L., Sillanpää, M., Häkkinen, A. (eds), IMWA Proceedings, Mine Water & Circular Economy (Vol I), Lappeenranta, Finland, 633–641.

Barnie, T.D., Oppenheimer, C., and Pagli, C., 2016a, Does the lava lake of Erta 'Ale volcano respond to regional magmatic and tectonic events? An investigation using Earth Observation data: Geological Society Special Publication, v. 420, p. 181–208, doi:10.1144/SP420.15.

Barnie, T.D., Keir, D., Hamling, I., Hofman, B., Belachew, M., Carn, S., Eastwell, D., Hammond, J.O.S., Ayele, A., Oppenheimer, C., Wright, T., 2016b. A multidisciplinary study of final episode of the Manda Hararo dyke sequence, Ethiopia, and implications for trends in volcanism during the rifting cycle. In: Wright, T.J., Ayele, A., Ferguson, D.J., Kidane, T., Vye-Brown, C. (eds), 2015. Magmatic Rifting and Active Volcanism, Geol. Soc. London, Sp. Publ. 420, 149–163, doi:10.1144/SP420.6.

Belachew, M., Ebinger, C., Coté, D., Keir, D., Rowland, J.V., Hamond, J.O.S., Ayele, A., 2014.

723 Comparison of dike intrusions in an incipient seafloor-spreading segment in Afar, Ethiopia:
724 seismicity perspectives. J. Geophys. Res. 116, B06405, doi: 10.1029/2010JB007908.

725 Bosworth, W., Huchon, P., McClay, K., 2005. The Red Sea and Gulf of Aden basins. J. African Earth Sci.
726 43, 334–378, doi:10.1016/j.jafrearsci.2005.07.020.

727 Corti, G., Molin, P., Sembroni, A., Bastow, I.D., and Keir, D., 2018, Control of Pre-rift Lithospheric
728 Structure on the Architecture and Evolution of Continental Rifts: Insights From the Main
729 Ethiopian Rift, East Africa: Tectonics, v. 37, p. 477–496, doi:10.1002/2017TC004799.

730 Ebinger, C., Ayele, A., Keir, D., Rowland, J., Yirgu, G., Wright, T., Belachew, M., Hamling, I., 2010.
731 Length and timescales of rift faulting and magma intrusion: the Afar rifting cycle from 2005 to
732 present. Annu. Rev. Earth Planet. Sci. 38, 437–64, 10.1146/annurev-earth-040809-152333.

733 Forslund, T., and Gudmundsson, A., 1991, Crustal spreading due to dikes and faults in southwest
734 Iceland: J. Struct. Geol. 13, 443–457, doi: https://doi.org/10.1016/0191-8141(91)90017-D.

735 Franzson, H., Helgadóttir, H.M., and Óskarsson, F., 2015. Surface exploration and first conceptual
736 model of the Dallol geothermal area, Northern Afar, Ethiopia. Proc. World Geotherm. Congress
737 2015, 11043, 11 p.

738 Golovin, A., Sharygin, V., Pokhilenko, N., Mal'kovets, V., Sobolev, N., 2003. Secondary melt inclusions
739 in olivine from unaltered kimberlites of the Udachnaya-Eastern pipe, Yakutia. Int. Kimberlite
740 Conf., Extended Abstr. 8., doi:10.29173/ikc3141.

741 Gonfiantini, R., Borsi, S., Ferrara, G., Panichi, C., 1973. Isotopic composition of waters from the
742 Danakil depression (Ethiopia). Earth Planet. Sci. Lett. 18, 13–21, doi: 10.1016/0012-
743 821X(73)90028-9.

744 Gressier, J.B., Mourgues, R., Bodet, L., Matthieu, J.Y., Galland, O., and Cobbold, P., 2010, Control of
745 pore fluid pressure on depth of emplacement of magmatic sills: An experimental approach:
746 Tectonophysics, v. 489, p. 1–13, doi:10.1016/j.tecto.2010.03.004.

747 Holwerda, J.G. Hutchinson, R.W., 1968. Potash-bearing evaporates in the Danakil area, Ethiopia.
748 Econ. Geol. 63, 124–150, doi: 10.2113/gsecongeo.63.2.124.

749 Hughes, G.W., Varol, O., Beydoun, Z.R., 1991. Evidence for Middle Oligocene rifting of the Gulf of
750 Aden and for Late Oligocene rifting of the southern Red Sea. Marine Petrol. Geol. 8, 354–358,
751 doi:10.1016/0264-8172(91)90088-I.

752 Jackson, M.P.A., Cornelius, R.R. Craig, C.H., Gansser; A., Stöcklin, J., and Talbot, C.J., 1990. Salt Diapirs
753 of the Great Kavir, Central Iran. Geol. Soc. Am. Mem. 177, 1-150 doi: 10.1130/MEM177-p1.

754 Keir, D., Pagli, C., Bastow, I.D., Ayele, A., 2011. The magma-assisted removal of Arabia in Afar :
755 evidence from dike injection in the Ethiopian rift captured using InSAR and seismicity. Tectonics
756 30, TC2008, doi:10.1029/2010TC002785.

757 Leroy, S., and 27 co-authors, 2012. From rifting to oceanic spreading in the Gulf of Aden: a synthesis.
758 Arab. J. Geosci. 5, 859–901, doi: 10.1007/s12517-011-0475-4.

759 Lister, J.R., 1990, Buoyancy-driven fluid fracture: The effects of material toughness and of low-
760 viscosity precursors: Journal of Fluid Mechanics, v. 210, p. 263–280,
761 doi:10.1017/S0022112090001288.

762 López-García, J.M., Moreira, D., Benzerara, K., Grunewald, O., López-García, P., 2020. Origin and
763 evolution of the halo-volcanic complex of Dallol: Proto-volcanism in Northern Afar (Ethiopia).
764 Frontiers Earth Sci. 17, https://doi.org/10.3389/feart.2019.00351.

765 Master, S., 2016. Gaet'ale- a reactivated thermal spring and potential tourist hazard in the Asale salt
766 flats, Danakil depression, Ethiopia. J. Appl. Volcanol. 5, 1, doi: DOI 10.1186/s13617-015-0042-x.

767 Mastin, L.G., and Pollard, D.D., 1988, Inyo Craters, Long Valley, California: Journal of geophysical
768 research, v. 93, p. 13,221-13,235.

769 Mège, D., and Korme T., 2004, Dyke swarms in the Ethiopian Large Igneous Province: not only a
770 matter of stress: J. Volc. Geotherm. Res. 132/4, 283-310, doi:10.1016/S0377-0273(03)00318-4.

771 Mège, D., Purcell, P.G., Bézos, A., Jourdan, F., La, C., 2015. A major dyke swarm in the Ogaden region
772 south of Afar and the early evolution of the Afar triple junction. In: Wright, T.J., Ayele, A.,
773 Ferguson, D.J., Kidane, T., Vye-Brown, C. (eds), 2015. Magmatic Rifting and Active Volcanism,
774 Geol. Soc. London, Sp. Publ. 420, doi:10.1144/SP420.7.

775 Moore, C., Wright, T., Hooper, A., and Biggs, J., 2019, The 2017 Eruption of Erta 'Ale Volcano,
776 Ethiopia: Insights Into the Shallow Axial Plumbing System of an Incipient Mid-Ocean Ridge:
777 Geochemistry, Geophysics, Geosystems, v. 20, p. 5727–5743, doi:10.1029/2019GC008692.

778 Moors, H., Honty, M., Smolders, C., Provoost, A., De Craen, M., and Leys, N., 2020. The waterbodies
779 of the Dallol volcano: A physico-chemical and geo-microbial survey, EGU General Assembly
780 2020, Online, 4–8 May 2020, EGU2020-1581, doi:10.5194/egusphere-egu2020-1581.

781 Nobile, A., Pagli, C., Keir, D., Wright, T., Ayele, A., Ruch, J., and Acocella, V., 2012. Dike-fault
782 interaction during the 2004 Dallol intrusion at the northern edge of the Erta Ale Ridge (Afar,
783 Ethiopia). Geophys. Res. Lett. 39, L19305, doi:10.1029/2012GL053152.

784 Pelloux, A., 1927. The minerals of Vesuvius. Am. Mineral. 12:14–21.

785 Perez, E., and Chebude, Y., 2017. Chemical analysis of Gaet'ale, a hypersaline pond in the Danakil
786 depression (Ethiopia): new record for the most saline water body on Earth. Aquat. Geochem.
787 23, 109-117, doi: 10.1007/s10498-017-9312-z.

788 Poppe, S., Galland, O., de Winter, N.J., Goderis, S., Claeys, P., Debaille, V., Boulvais, P., and Kervyn,
789 M., 2020, Structural and Geochemical Interactions Between Magma and Sedimentary Host
790 Rock: The Hovedøya Case, Oslo Rift, Norway: v. 21, 0–2 p., doi:10.1029/2019GC008685.

791 Rauche, H., van der Klauw, S., 2011. Resource report for the Danakhil potash deposit, Afar
792 State/Ethiopia. Technical report, ERCOSPLAN, Erfurt, Germany, 117 p.

793 Rauche, H., and van der Klauw, S., 2013, Resource Update for the Danakhil Potash Project, Danakhil
794 Depression, Afar State, Ethiopia. Technical report, ERCOSPLAN, Erfurt, Germany, 334 p.

795 Rauche, H., van der Klauw, S., 2015. Technical report in support of disclosure of preliminary
796 economic assessment for SOP production, Allana Potash Corp., Danakhil Project, Afar State,
797 Ethiopia. ERCOSPLAN, Erfurt, Germany, 268 p.

798 Roper, S.M., and Lister, J.R., 2007, Buoyancy-driven crack propagation: The limit of large fracture
799 toughness: Journal of Fluid Mechanics, v. 580, p. 359–380, doi:10.1017/S0022112007005472.

800 Sasvári, Á., and Baharev, A., 2014, SG2PS (structural geology to postscript converter) - A graphical
801 solution for brittle structural data evaluation and paleostress calculation: Computers and
802 Geosciences, v. 66, p. 81–93, doi:10.1016/j.cageo.2013.12.010.

803 Schofield, N., Alsop, I., Warren, J., Underhill, J.R., Lehné, R., Beer, W., and Lukas, V., 2014, Mobilizing
804 salt: Magma-salt interactions: Geology 42, 599–602, doi:10.1130/G35406.1.

805 Schultz, R.A., Mège, D., and Diot, H., 2008, Emplacement conditions of igneous dikes in Ethiopian
806 Traps: J. Volcanol. Geotherm. Res. 178, 683-692, doi:10.1016/j.jvolgeores.2008.08.012.

807 Talbot, C.J., 2008, Hydrothermal salt-but how much? Marine and Petroleum Geology, v. 25, p. 191–
808 202, doi:10.1016/j.marpetgeo.2007.05.005.

809 Wada, Y., 1992, Magma flow directions inferred from preferred orientaion of phenocrysts in a
810 composite feeder dike, Miyake-Jima, Japan: J. Volcanol. Geotherm. Res. 49, 119–126, doi:
811 10.1016/0377-0273(92)90008-2.

812 Warren, J.K., 2015, Danakhil Potash; Ethiopia - Modern hydrothermal and deep meteoric KCl, Part 3
813 of 4: Salty Matters, p. 1–9, doi:10.13140/RG.2.1.4883.3443.

814 Warren, J.K., 2016, Evaporites. A geological compendium: Springer, 1813 p., doi:10.1007/978-3-319-
815 13512-0.

816 Wolfenden, E., Ebinger, C., Yirgu, G., Deino, A., Ayalew, D., 2004. Evolution of the northern Main
817 Ethiopia rift: birth of a triple junction. Earth Planet. Sci. Lett. 224, 213–228,
818 doi:10.1016/j.epsl.2004.04.022.

819 Wright, T.J., Ebinger, C.E., Biggs, J., Ayele, A., Yirgu, G., Keir, D., Stork, A., 2006. Magma-maintained
820 rift segmentation at continental rupture in the 2005 Afar dyking episode. Nature 442, 291–294,
821 doi:10.1038/nature04978.

822 Wyrick, D.Y., Morris, A.P., Todt, M.K., and Watson-Morris, M.J., 2015, Physical analogue modelling of
823 Martian dyke-induced deformation: Geological Society Special Publication, v. 401, p. 395–403,
824 doi:10.1144/SP401.15.X

825 Xu, W., Xie, L., Aoki, Y., Rivalta, E., and Jónsson, S., 2020, Volcano-wide deformation after the 2017
826 Erta Ale dike intrusion, Ethiopia, observed zith radar interferometry: J. Geophys. Res. 125,
827 e2020JB019562, doi:10.1029/2020JB019562.

828

Figure 1.

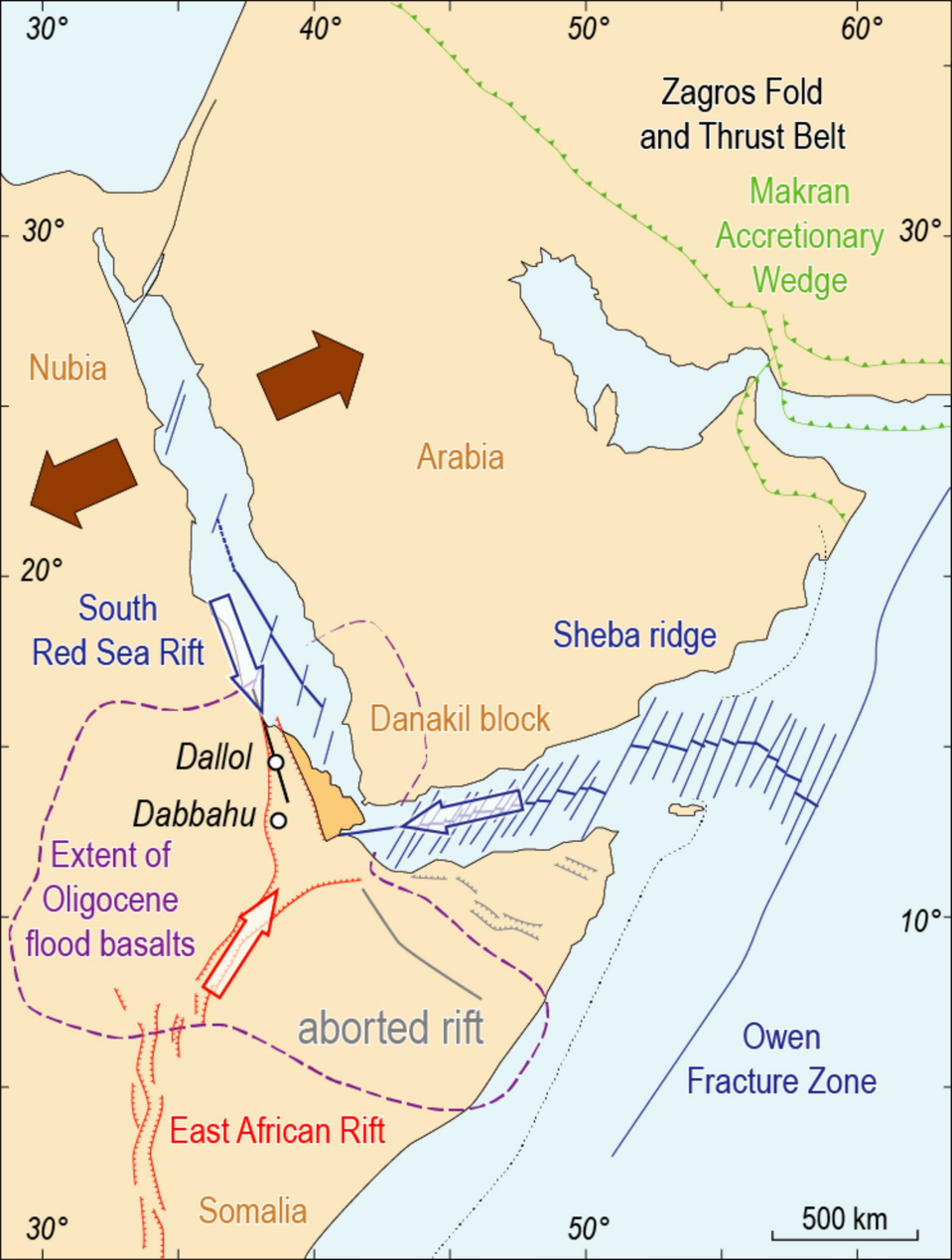
30°
40°
50°
60°
Zagros Fold
and Thrust Belt
Makran
Accretionary
Wedge
30°
30°
Nubia
Arabia
20°
South
Red Sea Rift
Sheba ridge
Danakil block
Dallol
Dabbahu
Extent of
Oligocene
flood basalts
aborted rift
10°
Owen
Fracture Zone
East African Rift
Somalia
30°
50°
500 km

Figure 2.

40°16’
40°18’
40°20’
40°22’
14°16’
14°14’
14°12’
14°10’
Fissure upflows
Putative Dallol sill boundary
Dallol Dome
Mogi source
Black Mountain
Yellow Lake
Yellow Lake Fissure
Black Mountain Dyke
Faults from seismics
Dallol - Erta Ale rift segment (Lake Karum/Asale)
4 km

Figure 3.

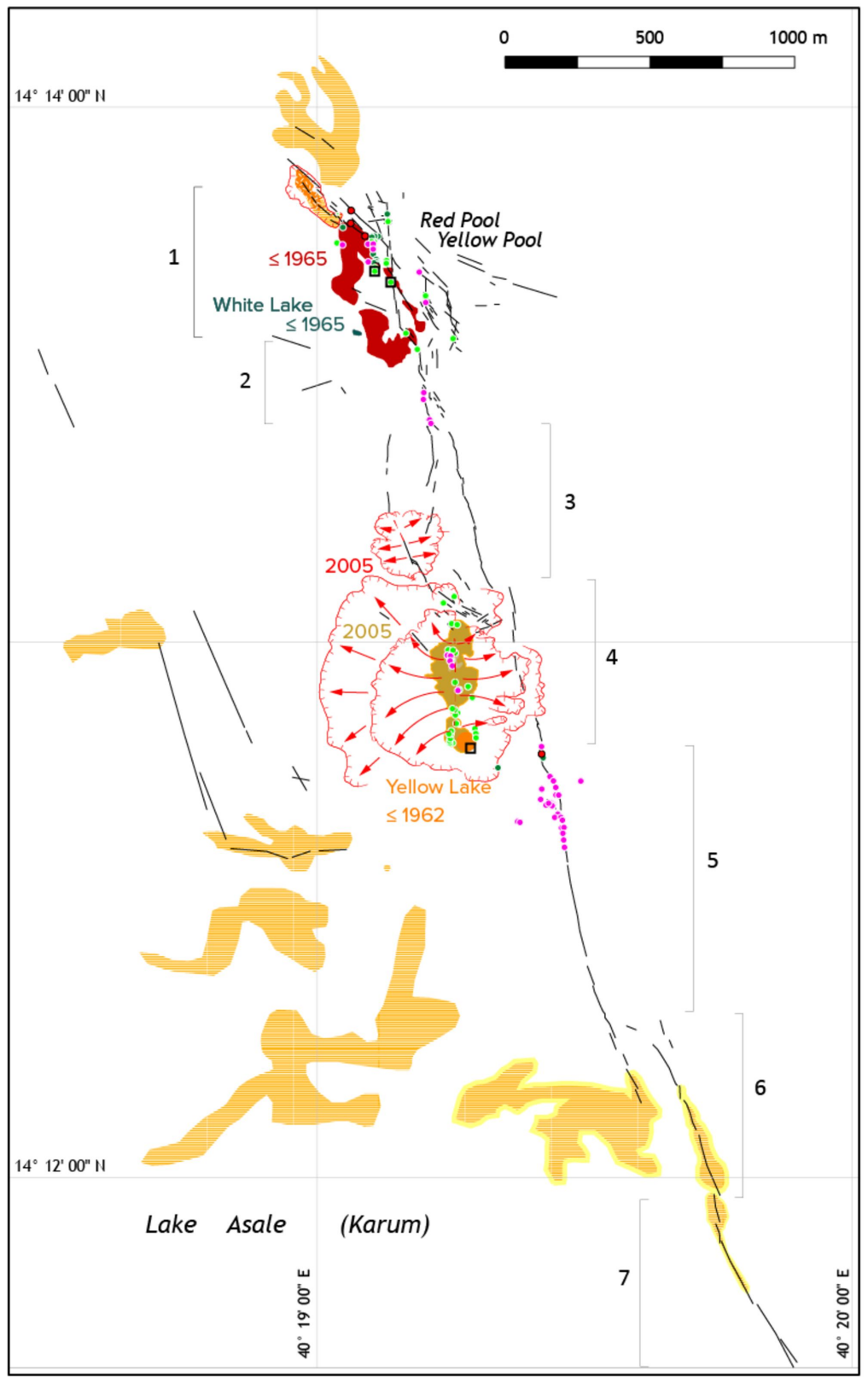

YELLOW LAKE FISSURE STRUCTURAL AND HYDROTHERMAL MAP

TECTONICS

- Fissure
- Covered resurfacing fissure (Yellow Lake area)

HYDROTHERMAL ACTIVITY

- Resurfacing lobe and sense of flow
- Red mud patch
- Native sulfur large concentration
- Area displaying circular native sulfur patches
- Native sulfur patch with white salt halo
- White Lake
- vent field
- Yellow Lake overflow
- Yellow Lake

POOLS AND BUBBLES

Shown larger than reality

- Active pool
- Dry pool
- Subsurface bubbling
- Bubbling dry pool

- Water sampling site

Figure 4.

Segment 1

Figure 5.

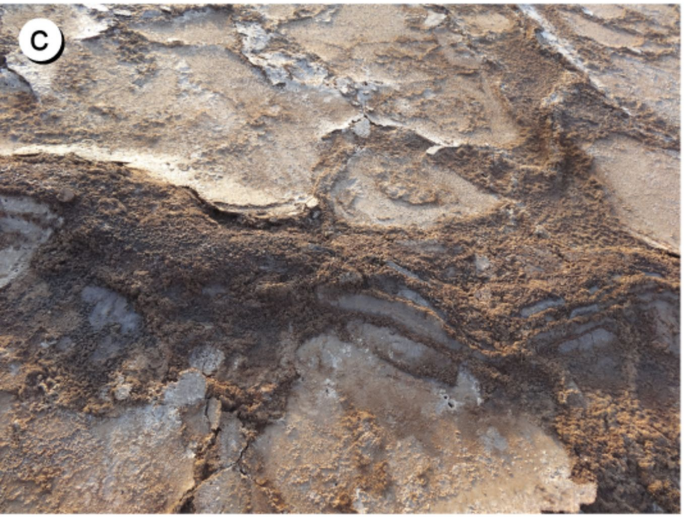

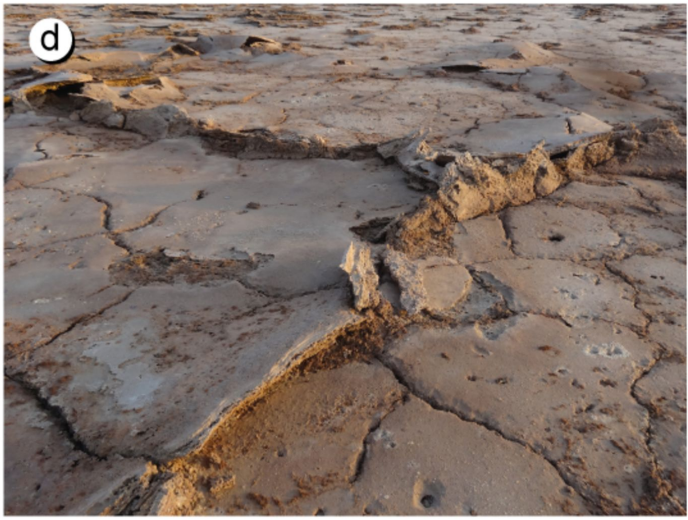

Segment 4

Figure 6.

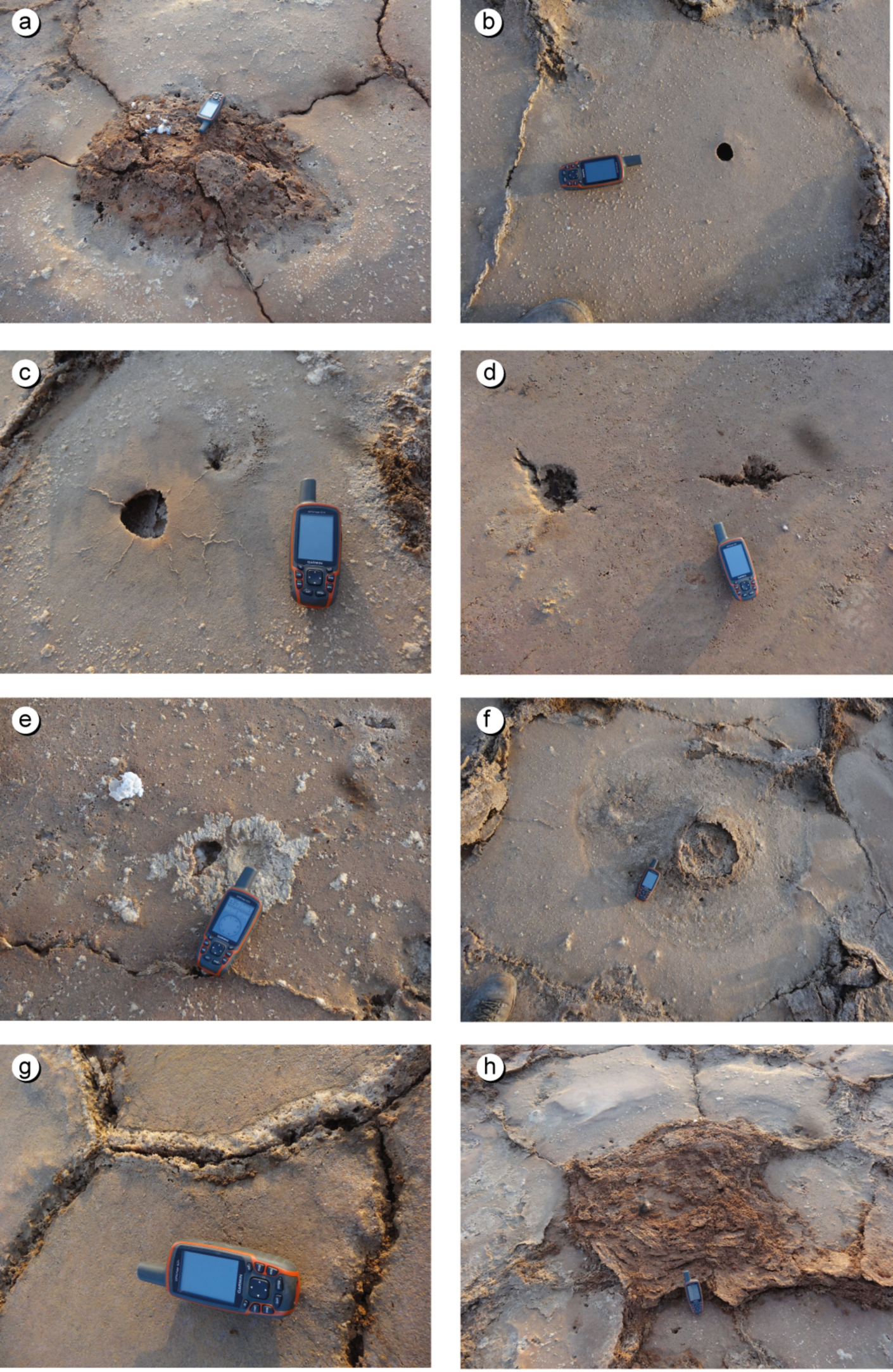

North of Yellow Lake

Figure 7.

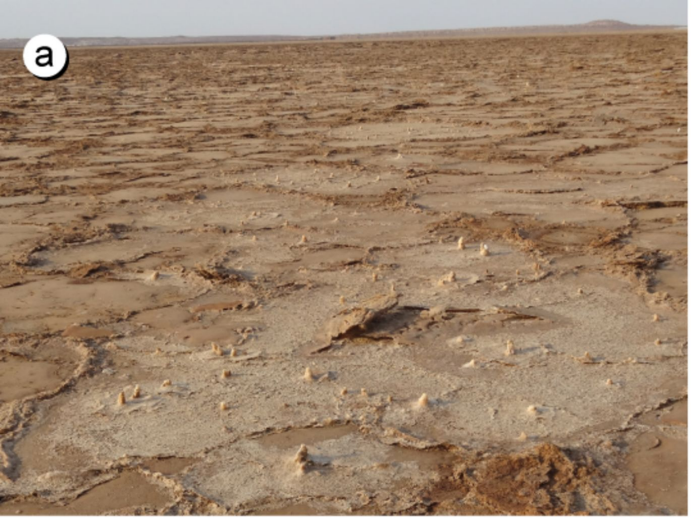

Segment 3 (West)

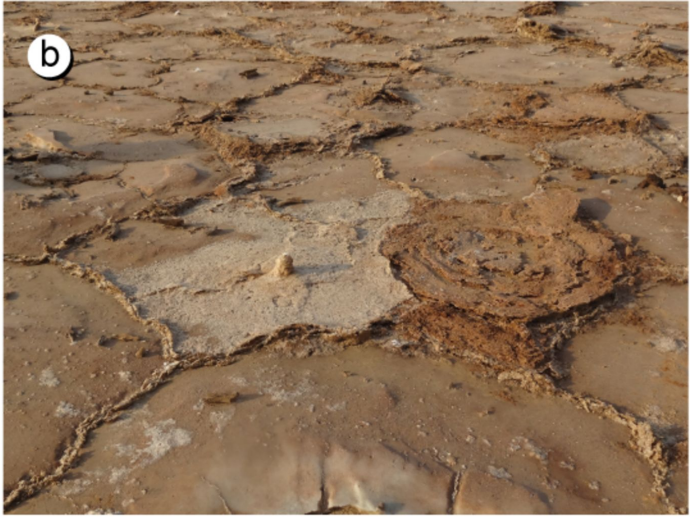

Segment 4

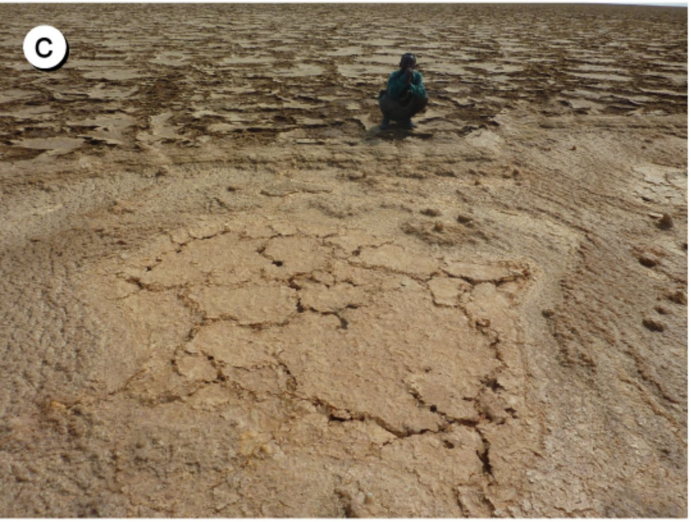

Segment 4

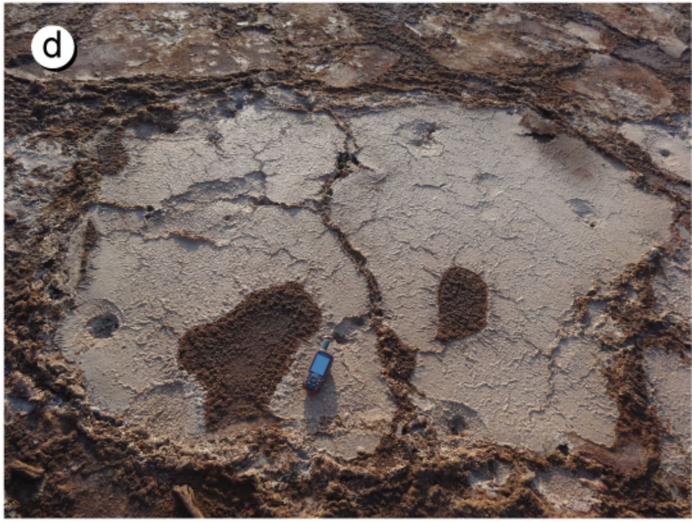

Segment 4

Figure 8.

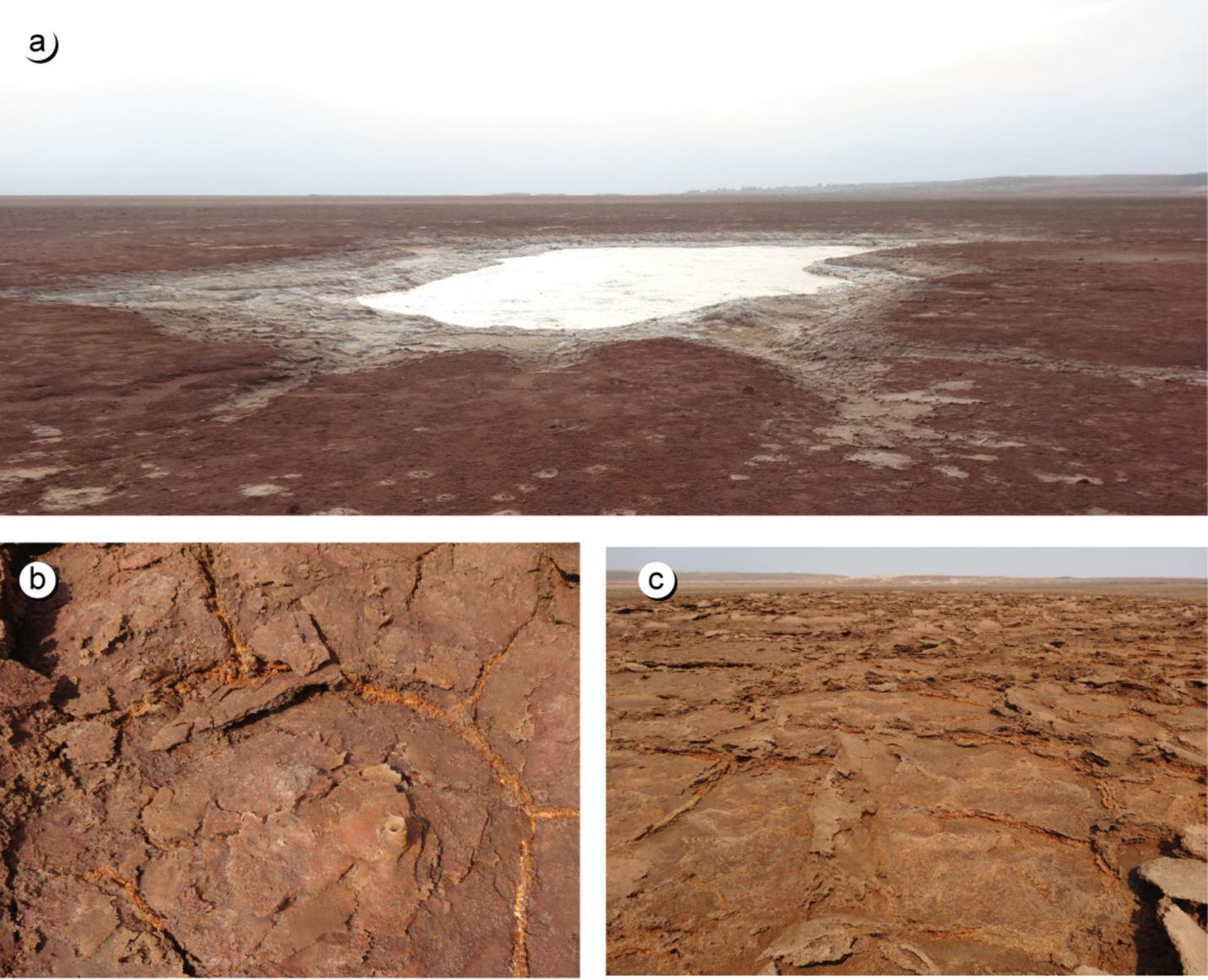

Segment 1

Figure 9.

Segment 1

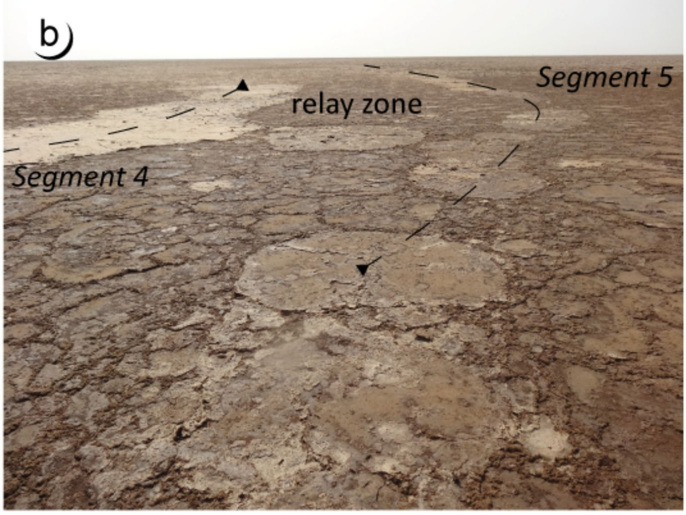

Segments 4-5

Segment 5

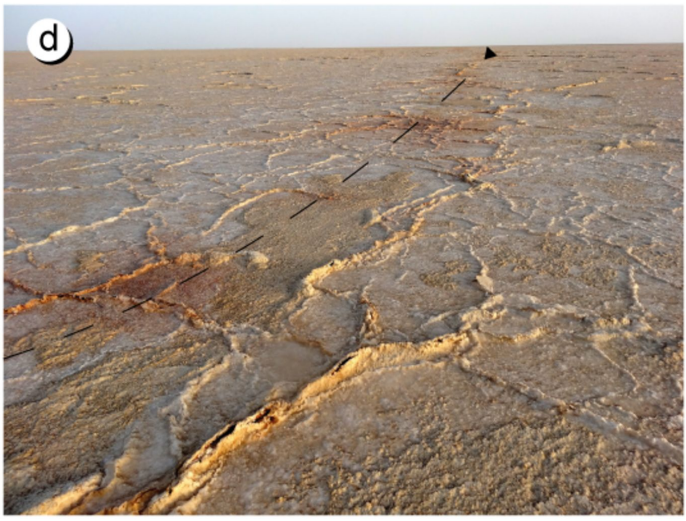

Segment 6

Segment 7

Relay zone, segments 6-7

Relay zone, segments 6-7

Figure 10.

a

b

c

14° 14' 00" N

14° 13' 00" N

14° 12' 00" N

40° 19' 00" E

40° 20' 00" E

YL

N117E

N165E

19-05-1965

02-06-2003

17-12-2005

0 500 1000 m

Figure 11.

a

1965 KeyHole 4-A 1965-05-19

Fracture strike frequency

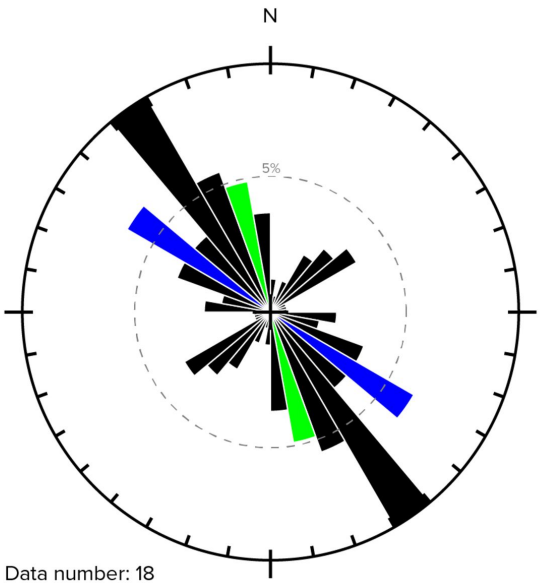

Data number: 18
Min length: 54 m
Max length: 446 m
Total length: 2445 m

Length-weighted fracture strike distribution

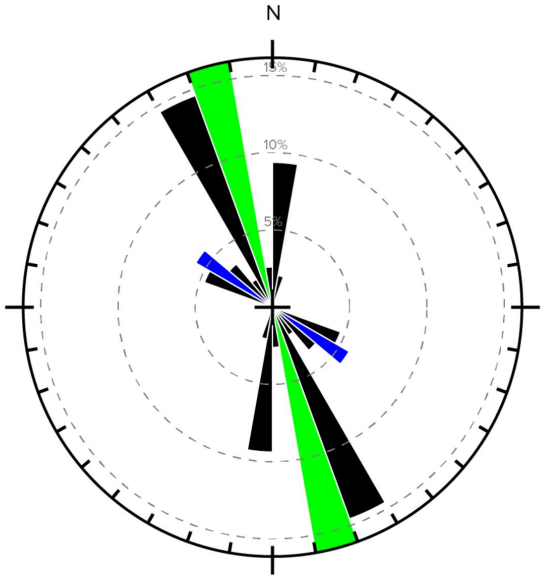

b

2003 Quickbird-2 2003-06-02

Fracture strike frequency

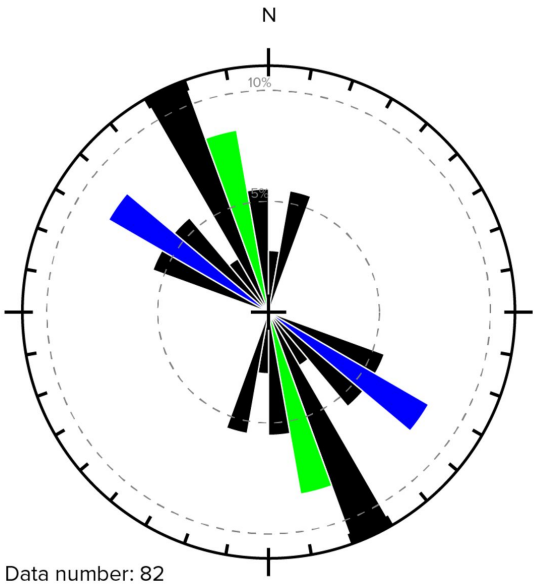

Data number: 82
Min length: 12.7 m
Max length: 129.0 m
Total length: 3404 m

Length-weighted fracture strike distribution

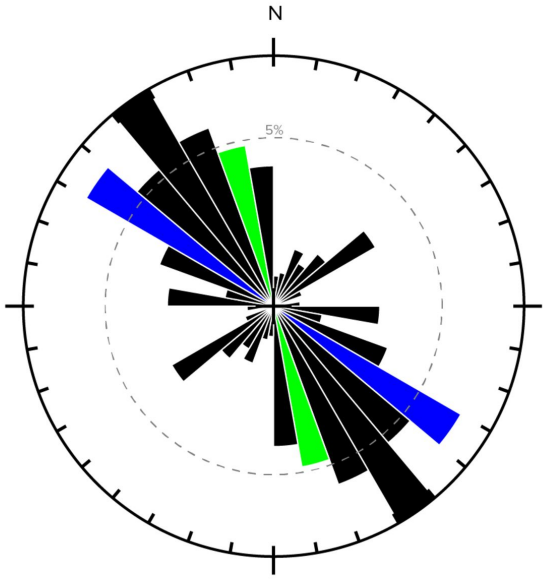

c

2005-2020 Since 2005-12-17 (OrbView-3)

Fracture strike frequency, YLF

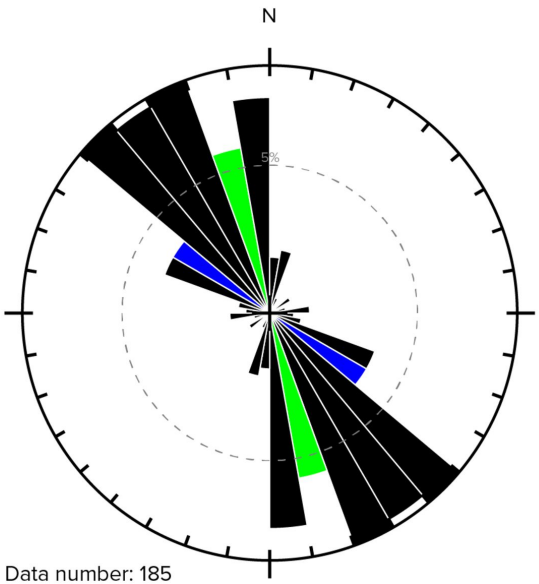

Data number: 185
Min length: 7.4 m
Max length: 319.3 m
Total length: 10037 m

Length-weighted fracture strike distribution, YLF

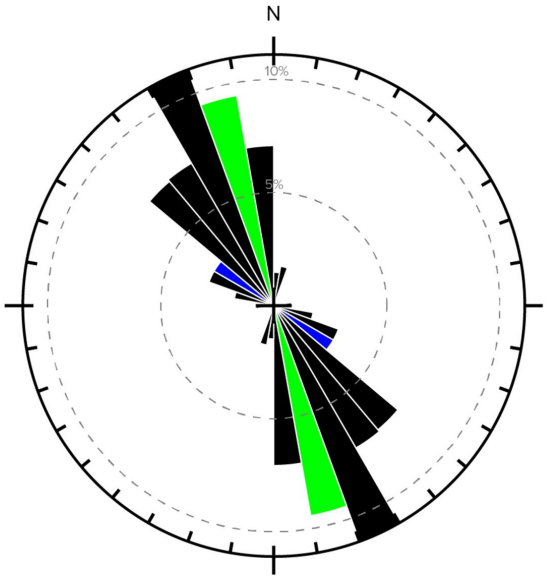

Figure 12.

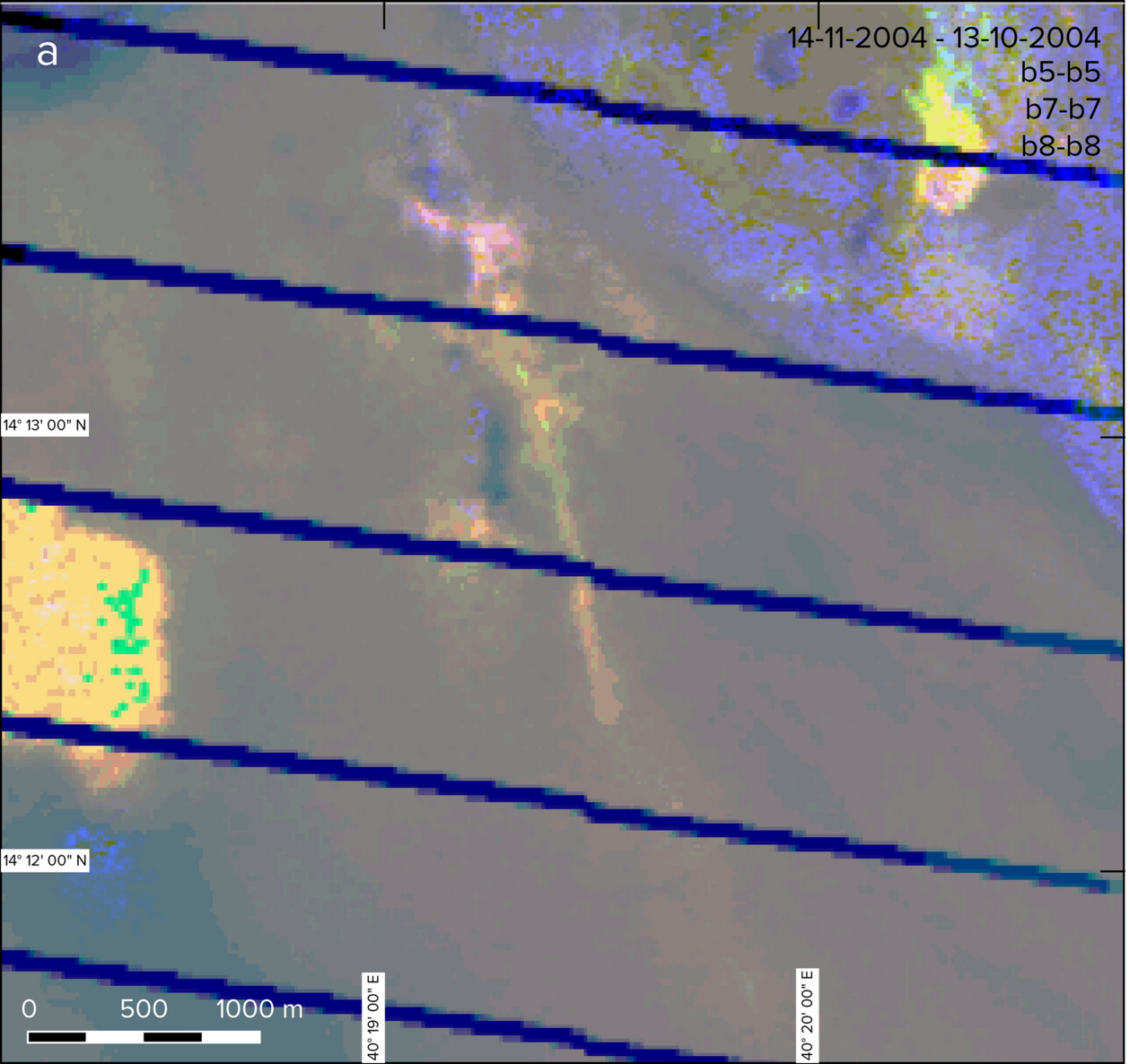
a
14-11-2004 - 13-10-2004
b5-b5
b7-b7
b8-b8
14° 13' 00" N
14° 12' 00" N
0
500
1000 m
40° 19' 00" E
40° 20' 00" E

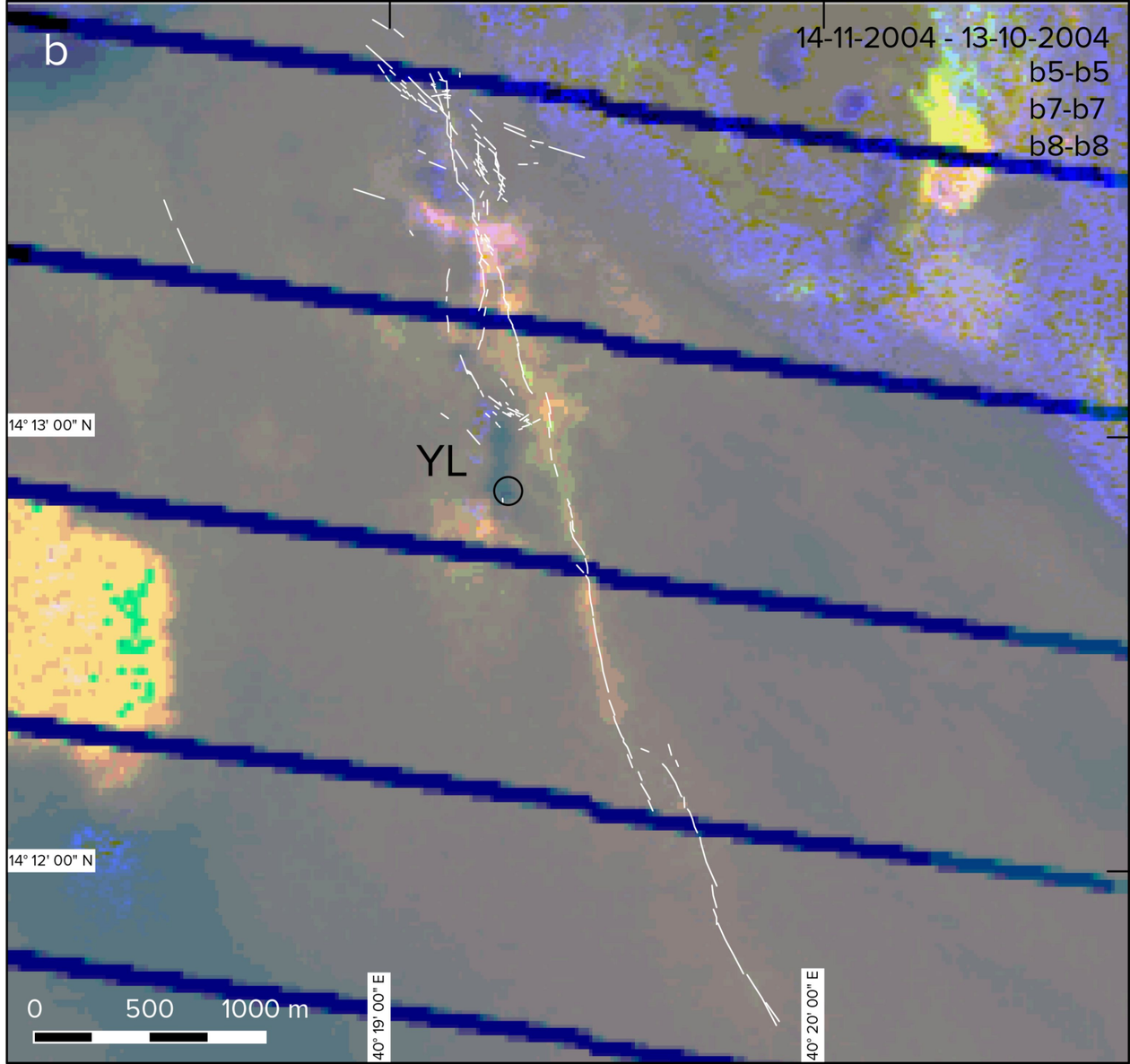
b
14-11-2004 - 13-10-2004
b5-b5
b7-b7
b8-b8
YL
14° 13' 00" N
14° 12' 00" N
0
500
1000 m
40° 19' 00" E
40° 20' 00" E

Figure 13.

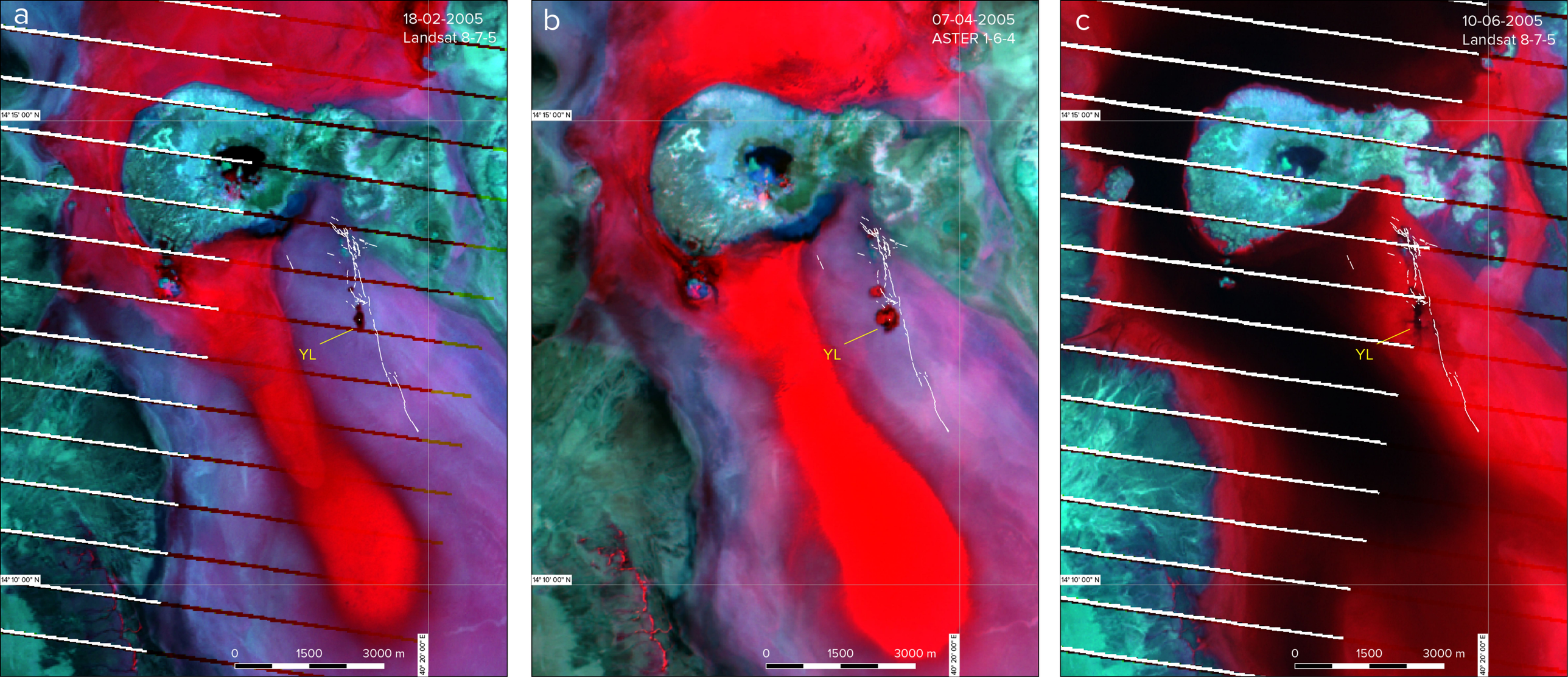
a
18-02-2005
Landsat 8-7-5
b
07-04-2005
ASTER 1-6-4
c
10-06-2005
Landsat 8-7-5
YL
14° 15' 00" N
14° 10' 00" N
40° 20' 00" E
0
1500
3000 m

Figure 14.

a

19-05-1965

Elevation (m)
-120.0
-126.2
-126.4
-126.5
-127.2
-133.5

0 150 300

b

21-10-2001
Landsat-7
b7-b4-B2 PS

0 150 300

c

02-06-2003

Elevation (m)
-120.0
-126.2
-126.4
-126.5
-127.2
-133.5

0 150 300

d

26-02-2019

Elevation (m)
-120.0
-126.2
-126.4
-126.5
-127.2
-133.5

0 150 300

Figure 15.

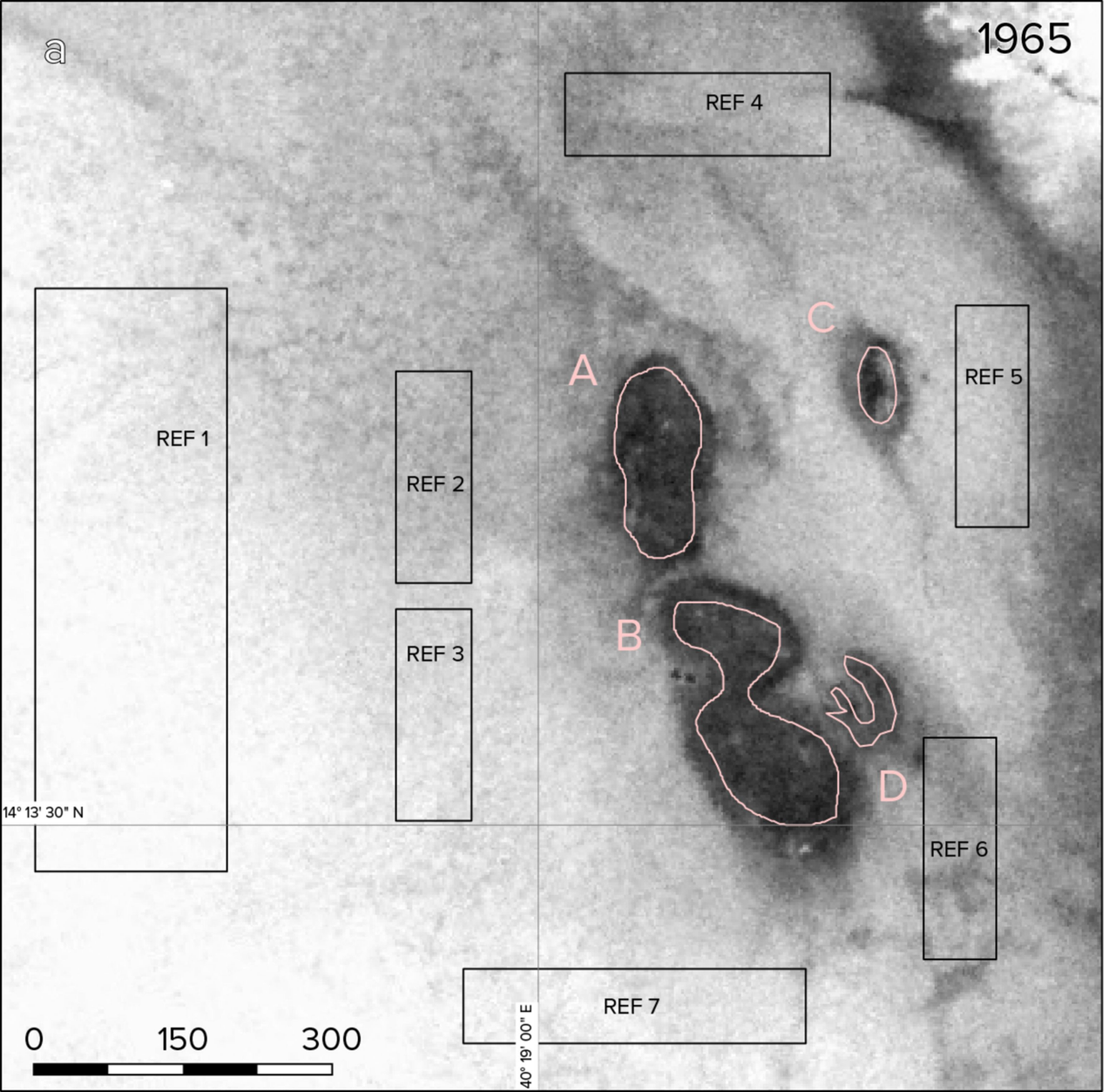
a
1965
REF 4
REF 1
REF 2
REF 3
REF 5
REF 6
REF 7
A
B
C
D
14° 13' 30" N
40° 19' 00" E
0
150
300

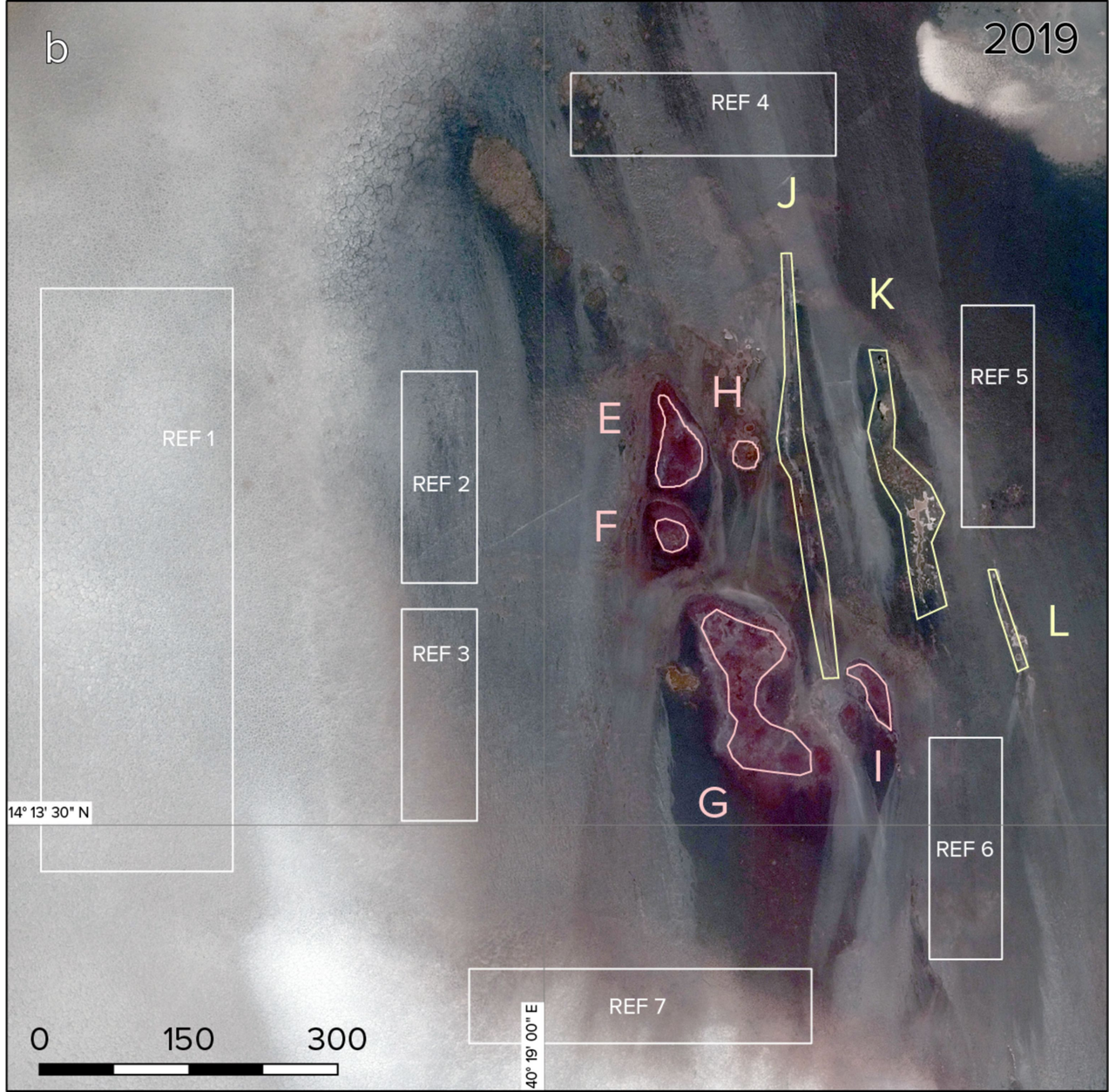
b
2019
REF 4
REF 1
REF 2
REF 3
REF 5
REF 6
REF 7
J
K
H
E
F
G
I
L
14° 13' 30" N
40° 19' 00" E
0
150
300

Figure 16.

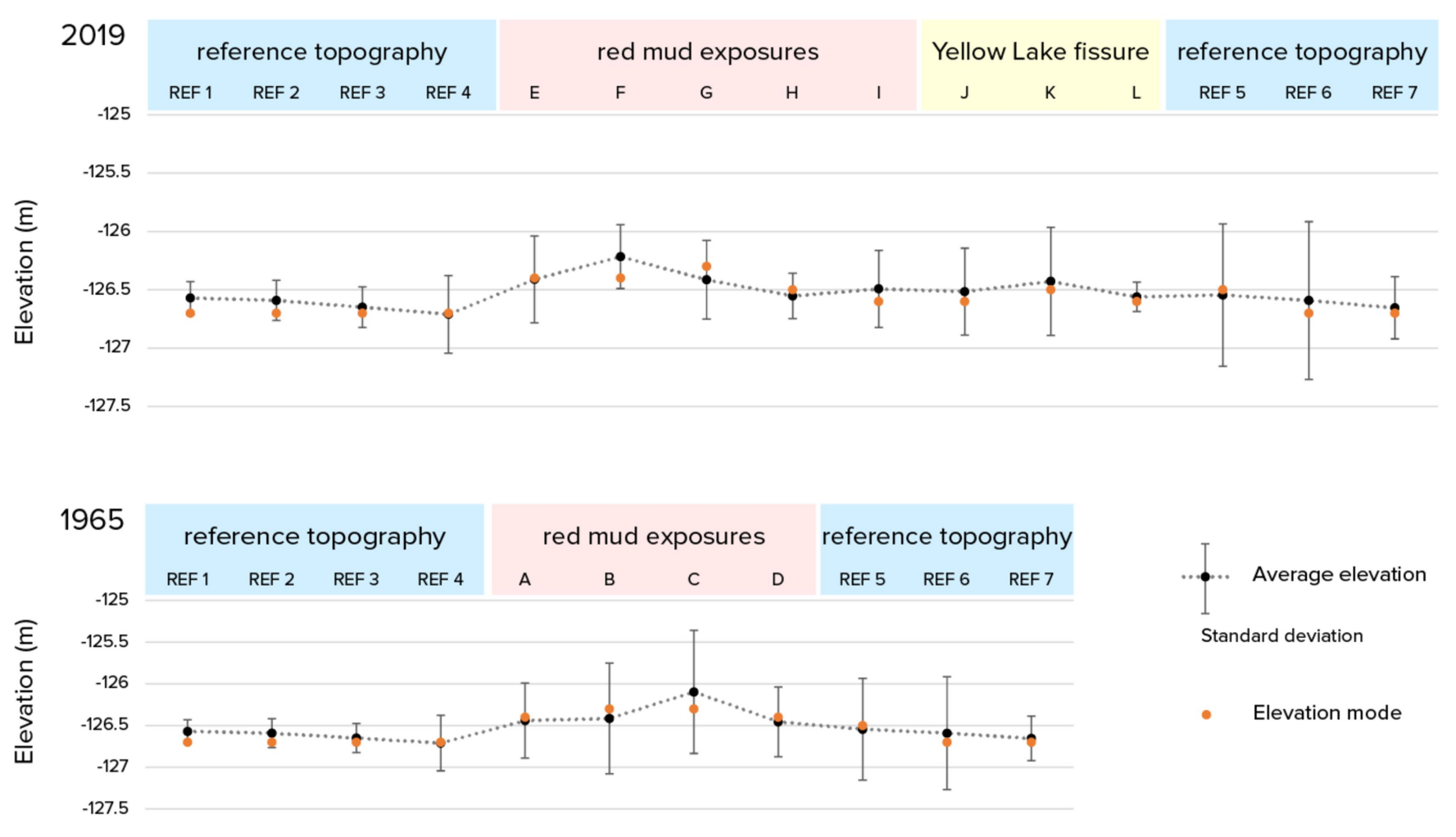
2019
reference topography
red mud exposures
Yellow Lake fissure
reference topography
REF 1
REF 2
REF 3
REF 4
E
F
G
H
I
J
K
L
REF 5
REF 6
REF 7
-125
-125.5
-126
-126.5
-127
-127.5
Elevation (m)
1965
reference topography
red mud exposures
reference topography
REF 1
REF 2
REF 3
REF 4
A
B
C
D
REF 5
REF 6
REF 7
-125
-125.5
-126
-126.5
-127
-127.5
Elevation (m)
Average elevation
Standard deviation
Elevation mode

Figure 17.

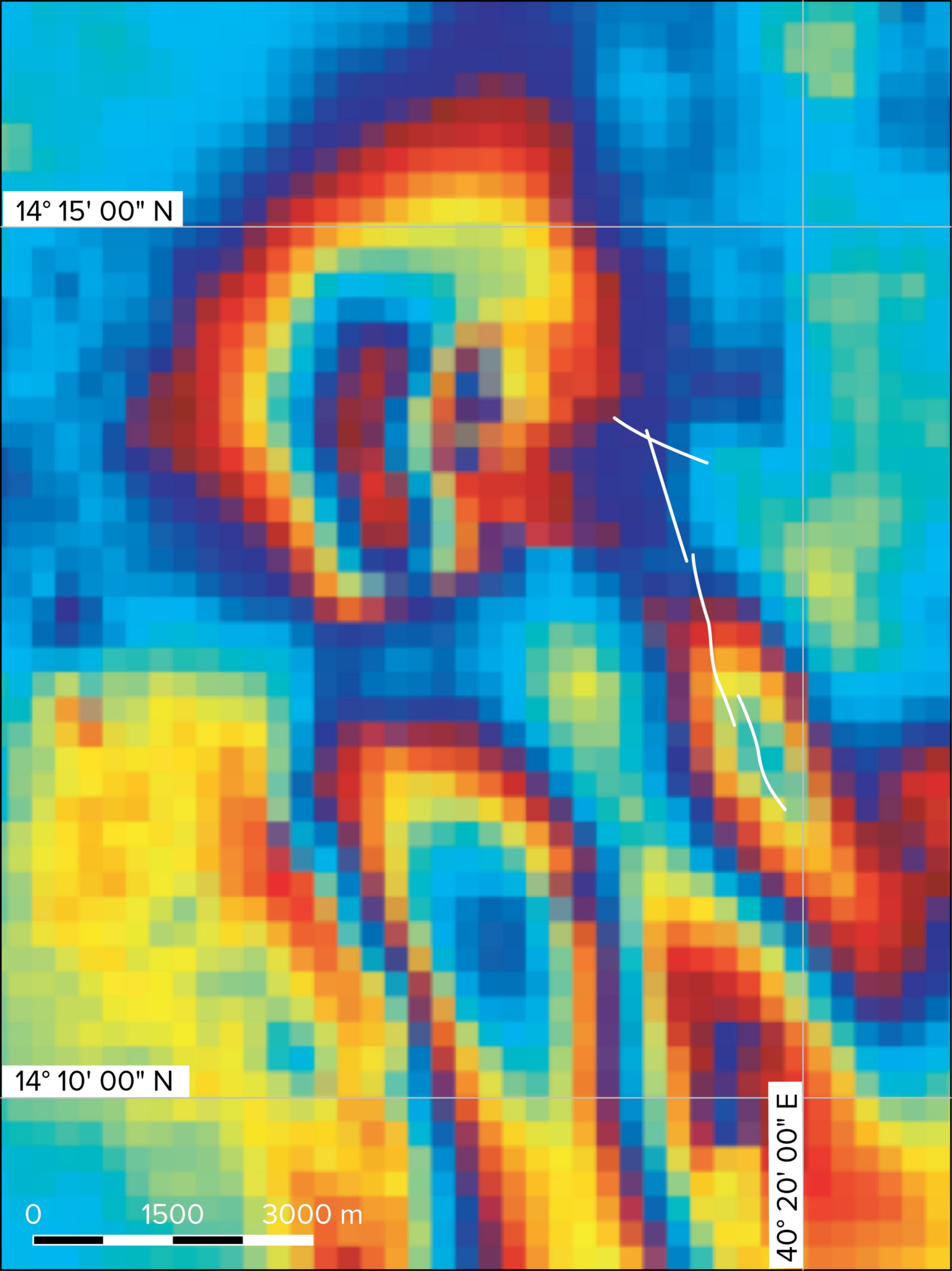
14° 15' 00" N
14° 10' 00" N
40° 20' 00" E
0
1500
3000 m

Figure 18.

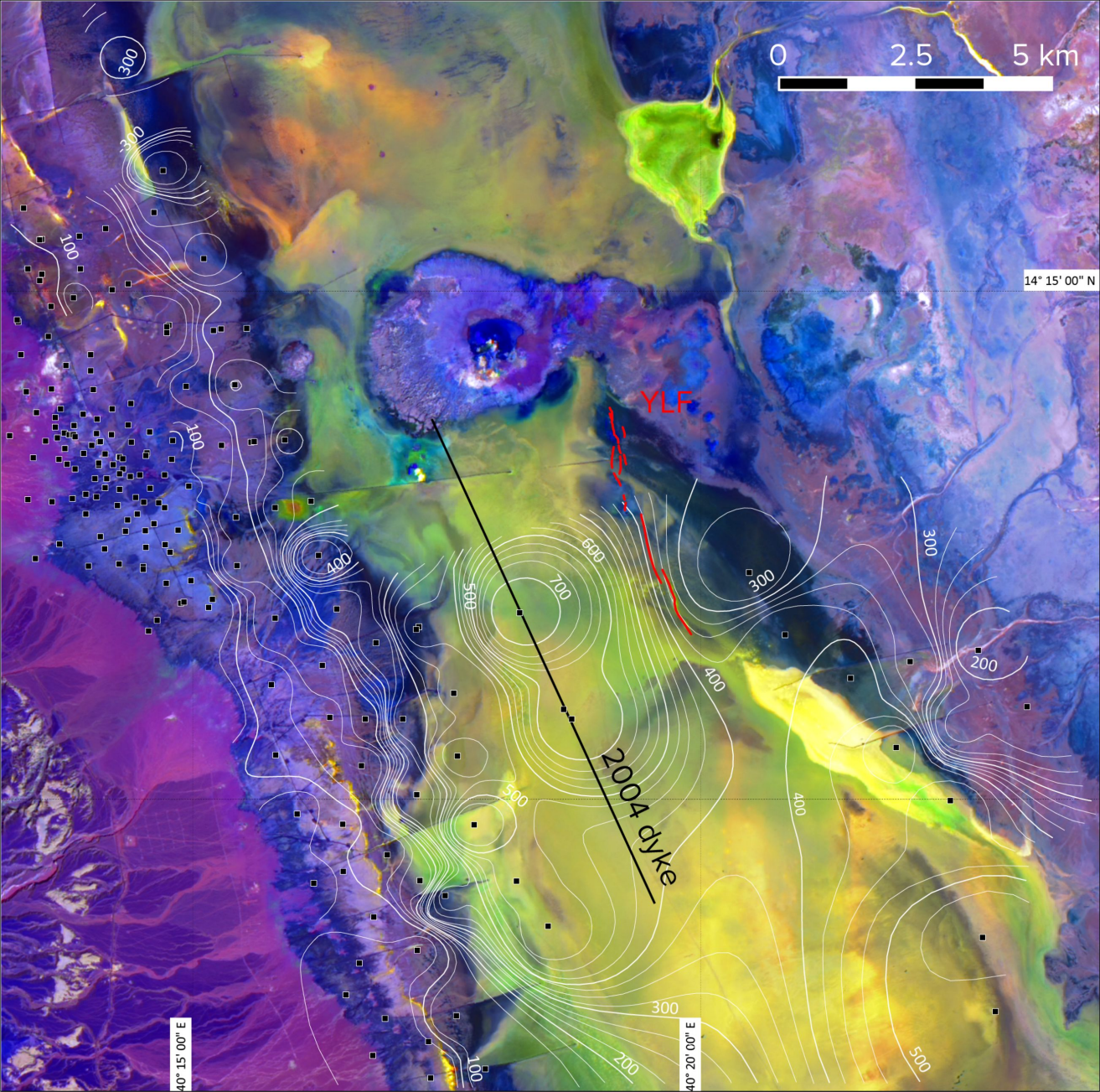
0
2.5
5 km
YLF
2004 dyke
14° 15' 00" N
40° 15' 00" E
40° 20' 00" E
100
200
300
400
500
600
700

Figure 19.

a

b

c

d

e